Multimodal transport and dispersion of organelles in narrow tubular cells

Saurabh S. Mogre and Elena F. Koslover*
Department of Physics, University of California San Diego, La Jolla, California 92093, USA

(Received 14 December 2017; published 3 April 2018)

Intracellular components explore the cytoplasm via active motor-driven transport in conjunction with passive diffusion. We model the motion of organelles in narrow tubular cells using analytical techniques and numerical simulations to study the efficiency of different transport modes in achieving various cellular objectives. Our model describes length and time scales over which each transport mode dominates organelle motion, along with various metrics to quantify exploration of intracellular space. For organelles that search for a specific target, we obtain the average capture time for given transport parameters and show that diffusion and active motion contribute to target capture in the biologically relevant regime. Because many organelles have been found to tether to microtubules when not engaged in active motion, we study the interplay between immobilization due to tethering and increased probability of active transport. We derive parameter-dependent conditions under which tethering enhances long-range transport and improves the target capture time. These results shed light on the optimization of intracellular transport machinery and provide experimentally testable predictions for the effects of transport regulation mechanisms such as tethering.

DOI: 10.1103/PhysRevE.97.042402

I. INTRODUCTION

Transport of cargo within the intracellular environment is a highly essential and tightly regulated process. Most eukaryotic cells have an active transport machinery consisting of molecular motors moving on a network of cytoskeletal polymers such as microtubules or actin filaments. Organelles can couple directly to motor proteins via specialized adaptors [1] or hitchhike on other motile organelles [2]. This mode of transport results in motion that is processive over variable length scales up to many microns. Many organelles execute bidirectional motion, switching direction between processive runs by either engaging alternate motor types or transferring to a cytoskeletal track with different orientation [3–7].

In addition to this motor-driven processive transport, effectively diffusive motion of organelles can arise due to thermal noise, active fluctuations of cytoskeletal networks [8], or hydrodynamic entrainment in flow set up by moving motors and cargo [9]. Evidence has shown that the short-time-scale movement of organelles appears effectively diffusive even when the underlying cytoplasmic medium is primarily elastic [8,10,11]. For brevity, we will refer to this stochastic motion of organelles as passive diffusion, while acknowledging that the fluctuations underlying the motion can have a number of actively driven origins.

The interplay between active and passive transport modes gives rise to length-scale-dependent effects. While processive transport is efficient at delivering cargo over long cellular distances, diffusion can more effectively spread organelles over smaller lengths. The balance between these transport modes has been quantified in previous work using the Péclet number, defined as $\mathrm{Pe} = vL/D$, where v is the processive velocity, L is the length scale of interest, and D is the diffusivity in the passive state [12]. High Péclet numbers correspond to lengths where active transport becomes dominant, assuming infinite processivity. In the case of finite processive run lengths, effectively diffusive behavior arises at long times as the particle executes many runs in randomly chosen directions [13,14].

While much previous work has relied on the mean square displacement (MSD) as a measure of particle spreading [13–15], this metric cannot be directly translated into quantities of biological relevance such as the rate of arrival to intracellular targets or particle interaction rates. Theoretical studies of first passage times by particles engaged in multimodal transport have demonstrated the existence of an optimum run length both in the absence of diffusion [16,17] and in the case where the particles can only interact with their target in the diffusive state [12,18,19]. These results suggest that the transport machinery in the cell may be optimized to allow substantial contributions from both processive and diffusive transport. In this work we focus on the relative importance of both passive and active transport modes to biologically relevant transport objectives, assuming organelles are functional in both states of motion. Endosomes, peroxisomes, lipid droplets, and mitochondria are some example organelles known to employ multimodal transport to move around within the cell while maintaining their function [20–23].

A variety of cellular processes rely on efficient transport to achieve distinct objectives necessary for biological function. One such objective is the establishment of a uniform distribution of particles throughout the cell, as is observed for peroxisomes, mitochondria, and lipid droplets [24–26]. Establishing this distribution, starting from the point of genesis of particular organelles, requires rapid transport and broad dispersion across long cellular length scales. Another objective is the delivery of organelles to specific subcellular regions. Examples include the motion of synaptic vesicles from the

*ekoslover@ucsd.edu

cell body to the presynaptic terminal of neuronal axons [27], and the transport of vesicles containing newly synthesized membrane-bound proteins from the Golgi apparatus to the cell boundary [28]. The role of different transport modes in this process depends on the length scale of separation between the site of organelle synthesis and their eventual target. A third cellular objective is the rapid encounter between an intracellular target and any one of a uniformly distributed population of organelles. For instance, peroxisomes serve to neutralize oxidative metabolic by-products, and the health of a cell is dependent on rapid removal of these toxic species as soon as they appear [29]. Similarly, early endosomes rely on contact with any of a population of lysosomes that aid in releasing the endosomal contents into the cytoplasm [30]. The efficiency of such a target encounter depends both on the nature of transport processes for the organelles and on their density within the cell.

The organization of the cytoskeletal network has a potentially important role to play in the distribution of intracellular particles. While a number of past models for intracellular transport employed a continuum approximation for cytoskeletal density [12,31,32], it is becoming clear that the specific arrangement of distinct cytoskeletal tracks has a substantial impact on cargo transport [33]. Obstructions due to intersecting microtubules may cause particles to pause or switch tracks and change the direction of movement [6]. Localized traps arising from heterogeneous filament polarity have been found to hinder transport in cell-scale computational models [33]. In tubular cell projections such as neuronal axons and fungal hyphae tips, the arrangement of cytoskeletal filaments is highly simplified, with microtubules aligned along the tubular axis and in many cases uniformly polarized towards the distal tip [34,35]. These projections range in length from tens to many hundreds of microns and require cargo to be efficiently transported from the cell body to the distal tips and back again. In addition to being particularly amenable to theoretical models of transport phenomena, these cell types are of fundamental biological importance. Defects in axonal transport in neurons have been implicated in a number of human pathologies, ranging from multiple sclerosis to Alzheimer's to prion diseases [36]. Due to their simplified morphology and long length, these tubular cells form an ideal system for investigating the length-scale-dependent effects of multimodal transport.

The discrete nature of cytoskeletal tracks within tubular cell projections limits active transport to narrow axially oriented bundles of microtubules [35]. It has been proposed in several cellular systems that transport efficiency is increased by directly tethering organelles to the microtubules in order to prevent them from losing access to the tracks [7,37,38]. Tethering can occur by specialized adaptor proteins binding the organelle to cytoskeletal tracks, as in the case for axonal mitochondria that become preferentially anchored in cellular regions with high metabolic needs [39–41]. Alternately, the binding of multiple motor proteins to individual vesicles results in a tethering effect that is believed to contribute to observed motor cooperativity [7,42]. Because tethering is expected to hinder short-range dispersion while enhancing the ability of organelles to engage in long-range processive walks, it can potentially serve as a regulatory mechanism for length-dependent transport.

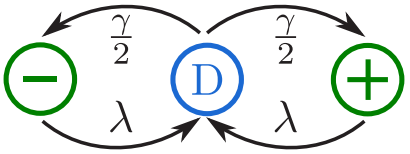

FIG. 1. Schematic for the transition between particle states. Here D denotes diffusive particles, + denotes particles moving in the rightward direction, and − denotes particles moving in the leftward direction. The arrows are labeled with transition rates between states.

In this article we present a simplified model for transport in a tube through a combination of processive walks and diffusion. We analyze the relative contributions of the two transport modes, as well as the possibility of tethering to cytoskeletal tracks, in achieving the different transport objectives of the cell. Section II establishes our halting creeper model and its behavior in terms of the rate with which particles explore a one-dimensional environment. In Sec. III we use the developed model to study the effects of bidirectional transport on distributing particles uniformly within a domain. In Sec. IV we explore the contribution of different transport modes to the delivery of individual particles, as well as target clearance by a dispersed particle population. Section V introduces an expanded model that accounts for particle tethering, delineating the effects of this mechanism on organelle dispersion and target capture times.

II. HALTING CREEPER MODEL

We define a simplified stochastic model for intracellular particles undergoing multimodal transport, focusing on motion along a single dimension. Each halting creeper particle exists in either a passive diffusive state characterized by diffusion coefficient D or an actively moving state with constant speed v in either the positive or negative direction (Fig. 1). Switching between the states is a Markovian process with constant starting rate γ for transitioning from the passive to the active state and constant stopping rate λ for transitioning from active to passive. Selection of the direction of motion is random at each initiation of an active run, and we assume complete symmetry between forward and backward motion. We note that this model is a more general form of previously defined creeping particle models [16], which have been analyzed in the limit $\gamma \to \infty$ and $D \to 0$. Furthermore, a three-dimensional version of our halting creeper model has previously been explored in the context of mean square displacement and local concentration fluctuations [12]. By contrast, in this work we focus explicitly on the efficiency with which such two-state transport distributes organelles throughout a cell and delivers them to intracellular targets.

Two important quantities which describe the behavior of a halting creeper particle are the active run length ($\ell = v/\lambda$) and the equilibrium fraction of particles in the active state ($f = \frac{\gamma}{\lambda+\gamma}$). For much of the subsequent discussion, we nondimensionalize all length units by the run length ℓ and all time units by the runtime $1/\lambda$. We define the remaining dimensionless parameters as $\hat{D} = \frac{D}{\ell^2\lambda}$, $\hat{\gamma} = \frac{\gamma}{\lambda}$, and dimensionless time $\hat{t} = \lambda t$.

The Markovian nature of the transitions between active and passive states allows the calculation of a spatiotemporal

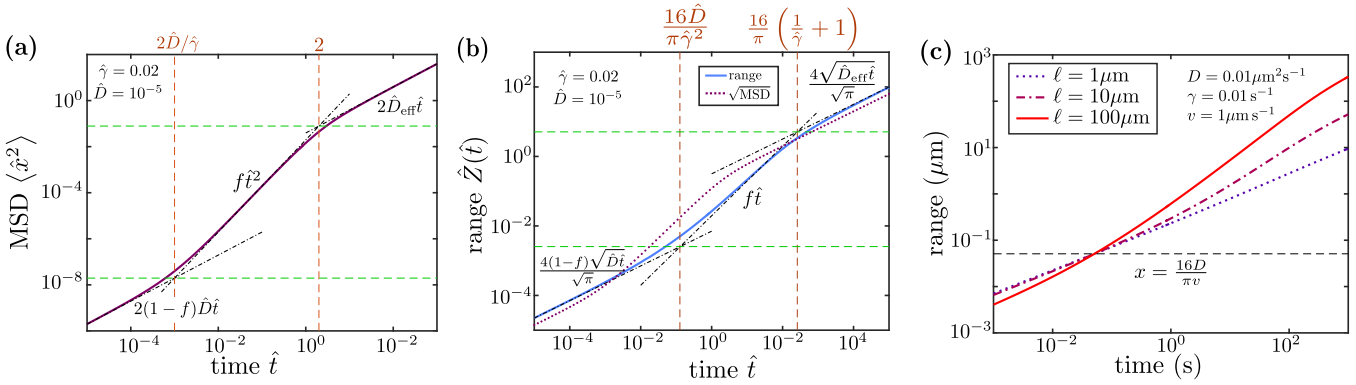

FIG. 2. Contribution of passive and active motion to spreading of particles at different length and time scales. (a) Mean square displacement for halting creepers. Black dash-dotted lines show scaling regimes. Vertical dashed lines indicate transition times between the regimes. Horizontal dashed lines indicate transition length scales. (b) Dimensionless range versus time for a halting creeper particle, with scaling regimes, transition times, and transition length scales indicated. The dotted curve shows the root mean square displacement for comparison. (c) Range versus time for typical parameter values for intracellular organelles, showing the increase in long-range transport with increasing run length, above a length scale indicated by the horizontal dashed line.

propagator function $G(x,t)$ for the halting creeper, which gives the distribution of positions at time t given the particle started at the origin at time 0. This propagator is obtained by convolution in the space and time domain of the individual propagators for passive and active transport. After a Fourier transform in space ($\hat{x} \to k$ and $G \to \tilde{G}$) and a Laplace transform in time ($\hat{t} \to s$ and $\tilde{G} \to \hat{\tilde{G}}$), the multimodal propagator for particles initially in an equilibrium distribution between passive and active states is given by

$$\hat{\tilde{G}}(k,s) = \frac{(\lambda+s)(\gamma+\lambda)(\gamma+\lambda+s) + (D\gamma(\lambda+s) + v^2\lambda)k^2}{(\gamma+\lambda)[s(\lambda+s)(\gamma+\lambda+s) + (D(\lambda+s)^2 + v^2(\gamma+s))k^2 + v^2Dk^4]}, \tag{1}$$

as derived in Appendix A. This propagator serves as the basis for our subsequent calculations on the efficiency of particle spreading and target site search.

A. Particle spreading: Mean square displacement

The MSD is a commonly used measure of spreading speed for diffusing particles. For the halting creeper model, it can be calculated directly from the propagator as

$$\langle \hat{x}(\hat{t})^2 \rangle = \mathcal{L}^{-1}\left[-\frac{\partial^2 \hat{\tilde{G}}}{\partial k^2}\bigg|_{k=0} \right] = 2(1-f)\hat{D}\hat{t} + 2f[\hat{t} + (e^{-\hat{t}} - 1)], \tag{2}$$

where the Laplace inversion $\mathcal{L}^{-1}$ is carried out analytically via the residue theorem.

This expression for the MSD is composed of a linear superposition of fraction $1-f$ of diffusing particles and fraction f of particles undergoing active walks that are persistent over a dimensionless time scale of 1. The latter component corresponds to an MSD that scales ballistically as $f\hat{t}^2$ for $\hat{t} \ll 1$ and diffusively as $2f\hat{t}$ for $\hat{t} \gg 1$. In the case of small diffusivity, there is an additional transition time when the ballistic motion begins to dominate over the passive diffusion. This occurs at $\hat{t}^* = \frac{2\hat{D}}{\hat{\gamma}}$. When $\hat{t}^* \ll 1$, the MSD transitions from diffusive to ballistic and back to diffusive scaling [Fig. 2(a)], as has previously been demonstrated with lattice models of mixed diffusive and processive transport [13]. The long-time behavior of the particle is defined by an effective diffusion coefficient

$$\hat{D}_{\rm eff} = (1-f)\hat{D} + f, \tag{3}$$

which in the limit of $\hat{t}^* \ll 1$ is dominated by the term corresponding to bidirectional active walks ($\hat{D}_{\rm eff} \to f$).

The relative importance of processive versus diffusive transport over a length scale x can be characterized by the Péclet number [12] $\mathrm{Pe}(x) = vx/D$, which is a dimensionless quantity often used to compare the contributions from advection and diffusion for particles in a flowing fluid [43]. A large Péclet number $\mathrm{Pe} \gg 1$ corresponds to transport that is dominated by the processive motion. In the case where active motion remains processive only up to distances comparable to the run length ℓ, the relevant Péclet number for long-range transport is $\mathrm{Pe}(\ell) = 1/\hat{D}$. Our dimensionless diffusion constant thus describes the relative contribution of diffusion above processive motion over a length scale comparable to the average run length. For the remainder of the discussion, we focus on the case where the transition time $\hat{t}^* = \frac{2\hat{D}}{\hat{\gamma}} < 1$ so that a distinct regime of processive motion appears between the regimes dominated by passive diffusion and effectively diffusive bidirectional walks. This is the case for the organelle transport examples listed in Table I. We note in passing that the presence of a discernible processive motion is key to identifying active runs

TABLE I. Estimated values of transport parameters for some biological systems. The run length can be obtained as $\ell = v/\lambda$. Parameters can be converted to dimensionless units according to $\hat{D} = D\lambda/v^2$, $\hat{\gamma} = \gamma/\lambda$, and $\hat{\rho} = \rho v/\lambda$.

Transport system	Rate of switching to active transport γ (s^{-1})	Rate of switching to passive transport λ (s^{-1})	Velocity of active transport v ($\mu m\, s^{-1}$)	Diffusivity D ($\mu m^2\, s^{-1}$)	Density of the population ρ (μm^{-1})	Approximate size of cellular region L (μm)
peroxisomes in fungal hyphae [24]	0.015[a]	0.29	1.9	0.014	1.5	50
lysosomes in kidney cells [6,44]	0.17	0.15	0.52	0.071		20
mouse neuron transport vesicles *in vitro* [45]	0.33[a]	2.7	0.8	0.03	0.14	
mitochondria in *Drosophila* axons [46]	0.17	0.15	0.35		1.3	1000
dense core vesicles in *Aplysia* neurons [47,48]	0.22[a]	2.2[b]	0.36[c]	0.002[c]	1.7	100
PrP^C vesicles in mouse axons [45,49]	0.36	0.15	0.85		0.4	100

[a]Estimated from the equilibrium fraction in the active state.
[b]Estimated from the single-particle trajectory.
[c]Estimated from the MSD plot.

in experimental particle-tracking data [24,47,50], so systems not in this regime are unlikely to be selected for studies of active transport.

B. Particle spreading: Range

An alternate metric for the efficiency of particle spreading is the overall range, the average size of the domain that has been explored by a halting creeper particle after an interval of time. For a one-dimensional model, the range of each particle is given by its maximum position minus its minimum position over the course of its trajectory. As will be discussed further in Sec. IV, the range is directly related to the rate at which a dispersed population of particles first encounters a target.

Our model permits calculation of the range over time for a halting creeper using the renewal equation method [16,51]. Namely, we define the distribution of first passage times to a target at position $x > 0$ (for a particle starting in a diffusive state at the origin) as $F_D(t;x) = F_{D+}(t;x) + F_{DD}(t;x)$, where F_{D+} gives the distribution of first passage times for the fraction of particles that arrive at the target while walking in the positive direction and F_{DD} gives the distribution of times for particles arriving in the passive diffusive state. Similarly, we consider the components of the propagator function defined in Appendix A, where $G_{DW}(x;t)$ gives the spatial distribution at time t of particles that began in a diffusive state at the origin at time 0 and are found in the actively walking state at time t. The other components G_{DD}, G_{WD}, and G_{WW} are defined analogously, with additional expressions for G_{+D} and G_{+W} giving the propagator for particles that are initially walking in the positive direction and end up in either the diffusive or the actively walking state. One of the renewal equations for this system is then given by

$$G_{DD}(x;t) = \int_0^t dt'[F_{DD}(t';x)G_{DD}(0;t-t') + F_{D+}(t';x)G_{+D}(0;t-t')], \quad (4)$$

A similar expression for purely processive bidirectional motion appears in [16]. In Eq. (4), the distribution of particles which start in the diffusive state and remain in the diffusive state $[G_{DD}(x;t)]$ comprises two terms, the first of which is a convolution between the probability that the particle first hits the target x at time t' in the diffusive state $[F_{DD}(t';x)]$ and the probability of it returning to position x within the remaining time $t-t'$, also in the diffusive state $[G_{DD}(0;t-t')]$. The second term includes a convolution between the probability that the particle first hits the target while walking forward $[F_{D+}(t';x)]$ and the probability that it returns to position x in the diffusive state $[G_{+D}(0;t-t')]$. Analogous renewal equations are derived for G_{DW}, G_{WD}, and G_{WW}.

After a Laplace transform in time, this convolution structure can be expressed as a product, which yields a system of equations

$$\begin{bmatrix} \hat{G}_{DD}(0) & \hat{G}_{+D}(0) \\ \hat{G}_{DW}(0) & \hat{G}_{+W}(0^+) \end{bmatrix} \begin{bmatrix} \hat{F}_{DD} \\ \hat{F}_{D+} \end{bmatrix} = \begin{bmatrix} \hat{G}_{DD}(x) \\ \hat{G}_{DW}(x) \end{bmatrix}, \quad (5)$$

where $\hat{F}$ and $\hat{G}$ denote the respective Laplace-transformed functions. Here $G_{+W}(0^+;t-t') = \lim_{\epsilon\to 0^+} G_{+W}(\epsilon;t-t')$ corresponds to the probability density for a particle that starts at time t' just before the origin walking in the positive direction to be at the origin and in a walking state at time t.

This system can be solved to calculate the first passage time $\hat{F}_D = \hat{F}_{DD} + \hat{F}_{D+}$ for particles that began in the diffusive state. Corresponding renewal equations for $G_{WD}(x;t)$ and $G_{WW}(x;t)$ yield the first passage time for particles that began in the active state:

$$\begin{bmatrix} \hat{G}_{DD}(0) & \hat{G}_{+D}(0) \\ \hat{G}_{DW}(0) & \hat{G}_{+W}(0^+) \end{bmatrix} \begin{bmatrix} \hat{F}_{WD} \\ \hat{F}_{W+} \end{bmatrix} = \begin{bmatrix} \hat{G}_{WD}(x) \\ \hat{G}_{WW}(x) \end{bmatrix}. \quad (6)$$

The range of the halting creeper particles over time ($Z(t)$) can be related to the Laplace transform of the overall first passage time $\hat{F}(s;x)$ according to [16]

$$Z(t) = \mathcal{L}^{-1}\left[\frac{1}{s}\int_{-\infty}^{\infty} \hat{F}(s;x)dx\right], \quad (7)$$

where $\hat{F}$ is a linear combination of $\hat{F}_D$ and $\hat{F}_W$, weighted by the equilibrium probability that the particle starts in an active or a passive state. To calculate the range function, we analytically perform the Fourier inversion of the propagators $\hat{G}_{DD}(0)$, $\hat{G}_{+D}(0)$, $\hat{G}_{DW}(0)$, and $\hat{G}_{+W}(0^+)$ by integrating over k. The spatial integral over x results in the right-hand side of the renewal equations being expressed as $\hat{\tilde{G}}_{DD}(k=0)$, etc. While short-time and long-time limits of the range can be obtained

directly from the large-s and small-s limits of the renewal equations, the relevant time scales for biological processes can span across many orders of magnitude, thus making it desirable to calculate the particle spreading efficiency over all time scales. To this end, we invert the Laplace transform numerically using Talbot's algorithm [52].

As shown in Fig. 2, the range exhibits similar transitions in scaling as the MSD. However, the transitions between the different regimes are shifted to longer times. At short times, the average range of particles with an equilibrium initial distribution between active and passive states can be calculated by solving the renewal equations in the limit $s \to \infty$ and performing the Fourier and Laplace inversions analytically for the lowest-order terms in $1/s$. The expression for the short-time average range is given (in dimensionless units) by

$$Z(\hat{t}) \to 4(1-f)\sqrt{\frac{\hat{D}}{\pi}}\sqrt{\hat{t}} + f\hat{t}. \tag{8}$$

Thus, the ballistic motion dominates over the diffusive motion above a critical transition time

$$\hat{t}^*_{\text{range}} = \frac{16\hat{D}}{\pi\hat{\gamma}^2}. \tag{9}$$

In the case where particles spend very little time in active motion ($\hat{\gamma} \ll 1$), this time scale is substantially longer than the transition time $\hat{t}^*$ for the MSD. The corresponding length scale for the transition from primarily diffusive to primarily ballistic motion is

$$\hat{x}^*_{\text{range}} = \frac{16\hat{D}}{\pi\hat{\gamma}(1+\hat{\gamma})}. \tag{10}$$

At longer times, there is a subsequent transition from the ballistic scaling of the range to the effectively diffusive long-time scaling

$$Z(\hat{t}) \to 4\sqrt{\frac{\hat{D}_{\text{eff}}}{\pi}}\sqrt{\hat{t}}, \quad \hat{t} \gg \hat{t}^{**}_{\text{range}}, \tag{11}$$

which occurs at a secondary transition time t^{**}_{range} and corresponding length scale x^{**}_{range} given by

$$\begin{aligned} \hat{t}^{**}_{\text{range}} &= \frac{16\hat{D}_{\text{eff}}}{\pi f^2}, \\ \hat{x}^{**}_{\text{range}} &= \frac{16}{\pi}\left(1+\frac{\hat{D}}{\hat{\gamma}}\right). \end{aligned} \tag{12}$$

In the case of a small fraction of time spent walking, this transition time is again shifted substantially above what would be expected from the MSD behavior, where the corresponding transition occurs at $\hat{t}^{**} = 2$. In the limit $\hat{D}/\hat{\gamma} \ll 1$, the transition time for the range can also be expressed as $\hat{t}^{**}_{\text{range}} = \frac{16}{\pi}(1 + 1/\hat{\gamma})$, comparable to the cycle time required for a single particle to transition between an active and a passive state and back again.

This result highlights the fundamental insufficiency of the MSD in describing the efficiency with which the particles explore their domain. Specifically, for a very small equilibrium walking fraction f, the time required for the active walks to contribute substantially to the average range can be well above the time scale $1/\gamma$ for an individual particle to start walking. Similarly, in this regime the range will only exhibit diffusive scaling at time scales long enough for individual particles to execute multiple starting and stopping transitions. Examples of particle motion where the pause time substantially exceeds the processive runtime include organelles (such as peroxisomes) whose active transport is mediated by hitchhiking on other organelles [2] and particles whose motion is driven by hydrodynamic entrainment due to cytoplasmic flow associated with nearby passing particles [9]. In such cases, the MSD does not accurately represent the rate at which these particles explore their domain.

We note that in the case where $\hat{D} < 1$, which corresponds to most biologically relevant examples, increasing the run length (e.g., by decreasing the stopping rate λ) raises the particle range for all length scales above $x > \frac{16D}{\pi v}$ (Fig. 2), corresponding to the length at which the Péclet number $\text{Pe}(x)$ becomes substantial. The implication is that longer processive runs improve the ability of particles to explore their domain at all length scales where active walks move faster than diffusion.

III. PARTICLE DISPERSION THROUGH BIDIRECTIONAL TRANSPORT

Having established the speed of particle spreading via multimodal bidirectional transport, we now turn to consider explicitly the efficiency with which such transport can achieve a particular cellular goal. Certain metabolic and regulatory needs of the cell require a well-dispersed distribution of organelles throughout the cell interior. For instance, mitochondria are found throughout neuronal axons, providing a locally available energy source through glucose metabolism [40]. In fungal hyphae, peroxisome organelles are maintained in a nearly uniform distribution [24], allowing for rapid neutralization of toxic metabolic by-products [29].

Establishing a well-mixed distribution relies not only on the ability of particles to move rapidly through the cell, but also on the ability of a transport mechanism to disperse and flatten regions of highly concentrated particles. We focus specifically on the rate with which a bolus of particles is spread over a cellular region. Such a process becomes necessary, for instance, in the case of rapid organelle production in response to an external signal, where the organelles must then be spread through long cellular projections such as axons or hyphae.

We use the halting creeper model to explore how different transport parameters affect the efficiency of such dispersion. Because we are interested in the initial establishment of an equilibrium spatial distribution, we consider particles that originate at $x = 0$ in the passive state, whose distribution is given by $G_D(x,t) = G_{DD}(x,t) + G_{DW}(x,t)$. This function can be evaluated by numerical Fourier-Laplace inversion of the transformed distribution, as described in Appendix A. The time evolution of the distribution is plotted in Fig. 3(a).

Note that long walk lengths result in little dispersion of particles, with the distribution splitting into two narrow, processively moving peaks. Short walk lengths lead to an effectively diffusive motion, with the particle distribution assuming the form of a slowly spreading Gaussian. An intermediate walk length combines both the rapid spreading of the distribution with the flattening of localized peaks to enable more efficient

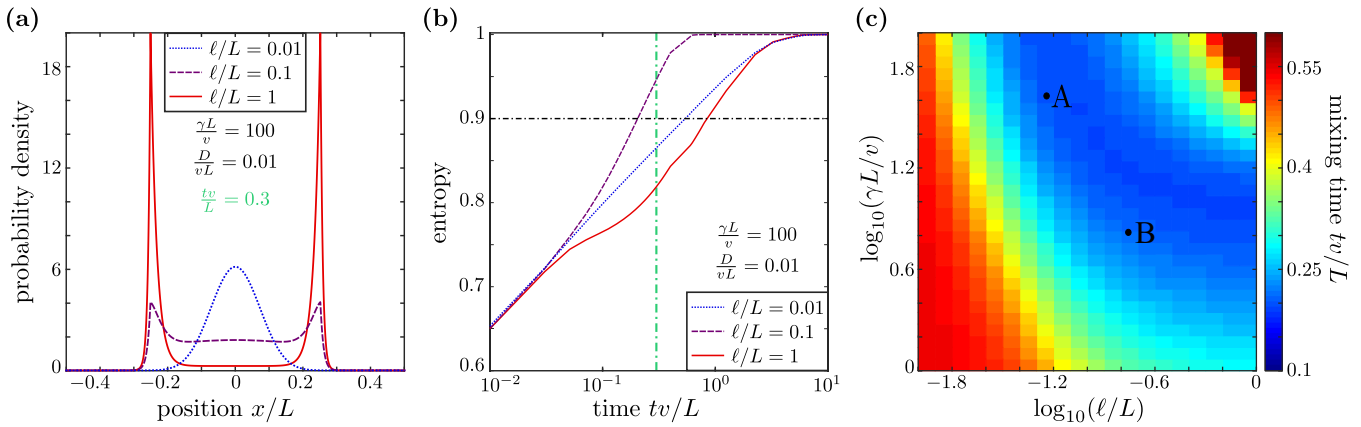

FIG. 3. Dispersion of particles towards a uniform distribution via bidirectional transport. All length units are nondimensionalized by domain length L and all time units by L/v. (a) Particle distribution density for different run lengths, at dimensionless time 0.3. (b) Entropy vs time for different run lengths. The horizontal dash-dotted line denotes the threshold entropy for the system to be considered well mixed. The vertical (green) dash-dotted line is at dimensionless time 0.3. (c) Time to reach a well-mixed state as a function of run length ℓ and rate of transition to an active state γ. Points A and B are drawn at corresponding transport parameters for lysosomes in monkey kidney cells and PrP^C vesicles in mouse axons, respectively (Table I).

dispersion. The limits for large and small walk lengths suggest that there exists an optimal run length ℓ for which the particles are most efficiently mixed.

A number of different metrics have been developed for quantifying the rate of mixing driven by stochastic processes [53–55], including several that track the approach of a bolus of particles towards uniform spread [56,57]. A commonality of these measures is their dependence on a particular length scale of interest [55] over which particles are to be mixed. For our one-dimensional system, we introduce a length L corresponding to the size of the domain on which uniform distribution is desired. This length represents the approximate extent of the tubular cell region across which particles are being dispersed. It can range over many orders of magnitude, with mammalian axons reaching up to a meter in length. Example values for some cellular systems are listed in Table I. We calculate the spatial distribution of halting creeper particles originating in the center of a domain of length L with reflecting boundary conditions, implemented using the standard image method [58]. The mixing of the particles is quantified via the Shannon entropy of the distribution [57,59], defined as

$$S = -\sum_{i=1}^{N} \frac{p_i \log(p_i)}{\log(N)}, \tag{13}$$

where the domain is broken up into N bins and p_i is the probability of a particle being located in bin i. Optimal mixing is achieved when the organelles are uniformly distributed, in which case $p_i = \frac{1}{N}$ and $S = 1$. Conversely, a distribution with all particles in a single section is the least mixed state, with $S = 0$. The entropy has an inherent dependence on the number of bins used for discretizing the probability distribution and we employ $N = 5000$ throughout our calculations.

The time evolution of the entropy is dependent on the dimensionless run length ℓ/L [Fig. 3(b)], with long runs corresponding to an initially slow rise in entropy as the bolus of particles evolves into two coherent spatial peaks until sufficient reversals are achieved to disperse the particles throughout the domain. Short run lengths limit the rate of entropy increase over long times, because the particle distribution spreads slowly as an effectively Gaussian peak. We consider the system to be well mixed when the entropy crosses a threshold value $S_t = 0.9$ and define the time taken to reach this state as the mixing time t_{mix}. This mixing time depends in a nonmonotonic fashion on both the starting rate γ and run length ℓ of processive walks [Fig. 3(c)]. High values of γ, corresponding to particles that spend most of their time in the active state, give rise to an optimum run length to achieve the most rapid mixing. This effect arises from the need to reverse the direction of active walks in order to efficiently disperse particles within the domain. However, each such reversal necessitates a waiting time of $1/\gamma$ during which the particles are in a passive state and spreading very slowly. Consequently, at low values of γ mixing is most efficiently achieved by particles that carry out very long walks. The results shown in Fig. 3 assume a small value of passive diffusivity ($\frac{D}{Lv} = 0.01$). Increasing this diffusivity would lead to a monotonic rise in the entropy, as diffusion enhances the particle mixing.

IV. TARGET SEARCH BY MULTIMODAL TRANSPORT

A. Search by a single particle

In addition to achieving uniform dispersion of particles, another goal of intracellular transport is to deliver organelles to specific cellular regions. This transport objective arises, for instance, when synaptic vesicles must reach the presynaptic bouton of a neuron [27]. Using our one-dimensional halting creeper model, we consider the first passage time of a single particle towards a stationary target located at distance x. For simplicity, we consider the case where x is much smaller than the overall extent of the domain so that the distance to the target x and the processive run length ℓ are the only relevant length scales in the problem. As in the case of our dispersion calculations (Sec. III), we consider particles that are initially in the passive state, as applicable to the distribution of newly synthesized organelles. The distribution of first passage times

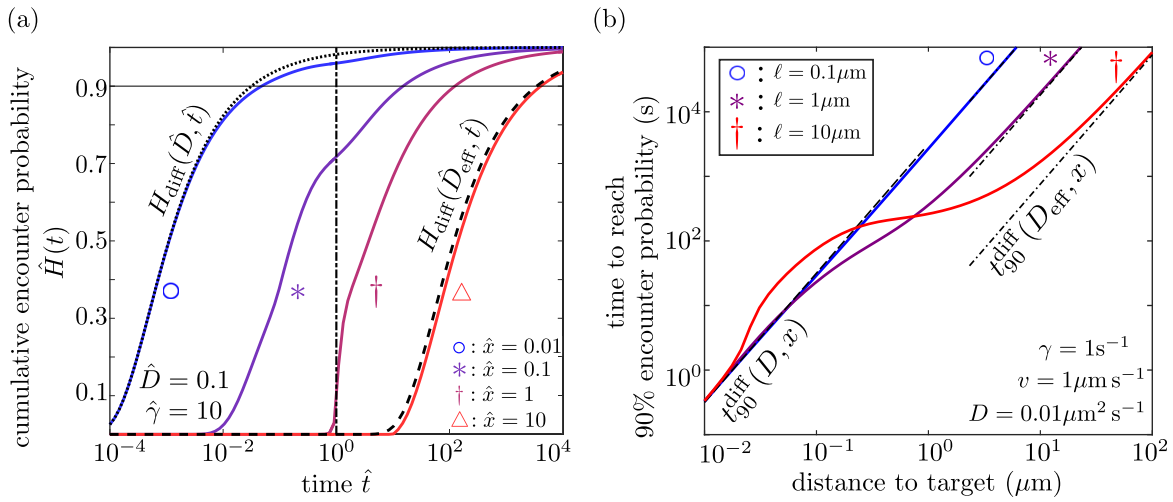

FIG. 4. Target capture times for a single particle. (a) Cumulative encounter probability for different initial distances to the target $\hat{x}$. The dotted and dashed lines denote the encounter probability for diffusive particles with diffusion coefficients $\hat{D}$ and $\hat{D}_{\rm eff}$, respectively. The dash-dotted line denotes the average time required for a particle in the active state to cover a distance of $\hat{x}=1$. All length units are nondimensionalized by ℓ and all time units by ℓ/v. (b) Time to reach 90% capture probability for different run lengths, assuming a rapid starting rate $\gamma=1\ {\rm s}^{-1}$ and distances appropriate for intracellular organelle transport. The dotted and dashed lines denote $t_{90\%}$ for diffusive particles with diffusion coefficients $\hat{D}$ and $\hat{D}_{\rm eff}$, respectively.

can be obtained from the renewal equation (5) by carrying out analytic Fourier inversion followed by numerical Laplace inversion of the propagators (see Appendix A).

The cumulative distribution of encounter times to the target is plotted in Fig. 4(a), showing the transition from a passively diffusive process at small distances ($\hat{x}<x^*_{\rm range}$) to an effectively diffusive process (with diffusivity $\hat{D}_{\rm eff}$) at distances much longer than the run length ($\hat{x}>1$). For comparison, the cumulative distribution for a purely diffusive process is given by

$$H_{\rm diff}(\hat{x},\hat{t};\hat{D})=1-{\rm erf}\left[\frac{\hat{x}}{\sqrt{4\hat{D}\hat{t}}}\right]. \tag{14}$$

By contrast, intermediate distances show a sharp increase in the cumulative probability of target encounter at time $\hat{t}=\hat{x}$, corresponding to the arrival of the first processively walking particles.

Because the average first passage time of a random walk in a semi-infinite domain diverges [58], we focus on the time required for particles to hit the target with sufficiently high probability. Analogous to our calculations of particle dispersion in Sec. III, we define the hitting time $t_{90\%}$ as the time by which there is a 90% chance that the particle has hit the target. We note that $t_{90\%}$ is well defined even on a semi-infinite domain due to the recurrent nature of random walks in one dimension, ensuring a finite hitting time for all particles [58]. For short distances, the time for probable encounter of the particle scales as expected for purely diffusive motion with diffusivity $\hat{D}$ [Fig. 4(b)],

$$t_{90}^{\rm diff}(\hat{x};\hat{D})=\frac{\hat{x}^2}{4\hat{D}[{\rm erf}^{-1}(0.1)]^2}, \tag{15}$$

where erf is the error function. At long times, a similar scaling is observed with effective diffusivity $\hat{D}_{\rm eff}$.

As is the case when the transport objective is to achieve a uniform distribution of particles, increasing the length of processive runs does not necessarily result in more efficient transport. This is true despite the fact that, unlike previous models of multimodal transport [12,18,19], we consider our particles capable of accessing their target in both the passive and active states. A run length that is much longer than the distance to the target can hinder particle delivery, because particles have a 50% chance of initiating their motion in the wrong direction. They then require a long time to stop, turn, and return towards the target. At the same time, very short processive runs decrease the overall rate of spread for the particle distribution and thus slow down the target encounter. These two effects give rise to an optimum in the efficiency of target delivery, with minimal values of target hit time $t_{90\%}$ occurring at intermediate run lengths ℓ [Fig. 4(b)]. This effect is a direct analog to the optimum walk length for achieving uniform distribution. The existence of this optimum walk length has also previously been noted for creeper models without any paused or passive state [16,17].

We additionally provide a calculation of first passage times in the alternate case where the particle is capable of accessing its target in the passive state only (see Appendix B). In such a system, the optimal walk length decreases substantially compared to the model where both states are functional, as the rapid processive transport must be counterbalanced by sufficient time spent in the passive regime in order to capture the target. This effect is distinct from the disadvantage of long walks which can lead the particle away from its target, underlying the nonmonotonic dependence on ℓ in Fig. 4.

B. Search by a population of particles

A closely related objective of intracellular transport is the capture of a target by any one of many moving particles. In this case we assume particles that are initially uniformly

distributed with some density ρ and consider the mean first passage time (MFPT) for the first of them to hit the target. Some biological examples include the clearance of toxic cytoplasmic metabolites by any one of a uniformly scattered field of peroxisome organelles [29], the influx of peroxisomes to plug septal holes in damaged fungal hyphae [60], or the arrival of lysosomes to fuse with a phagosome and digest its engulfed contents [30]. For simplicity, we assume the target is itself immobile and must wait for the particles to come to it via some combination of active and passive transport. In this situation, the relevant length scale is defined by the typical initial spacing between the particles ($1/\rho$). In the limit of a uniform distribution over a very long domain, the MFPT can be related directly to the range of the moving particles [16]. Specifically, the mean first passage time is given by

$$\mathrm{MFPT} = \int_0^\infty e^{-\rho Z(t)} dt, \tag{16}$$

where $Z(t)$ is the average range of particles over time t.

The behavior of the MFPT is dictated by the dimensionless length scale for the separation between particles ($1/\hat{\rho} = 1/\rho\ell$). When this length scale is short enough that active walks remain processive ($1/\hat{\rho} \ll \hat{x}^{**}_{\mathrm{range}}$), we can approximate the particle range as a linear combination of a diffusive and a ballistic process. The MFPT can then be calculated analytically by plugging Eq. (8) into Eq. (16) and integrating the resulting exponential

$$\mathrm{MFPT} \approx \frac{1}{f\hat{\rho}} - \sqrt{\frac{4\hat{D}}{\hat{\gamma}^2\hat{\rho}f}}\exp\left[\frac{\hat{x}^*_{\mathrm{range}}\hat{\rho}}{4}\right]\mathrm{erfc}\left[\frac{\hat{x}^*_{\mathrm{range}}\hat{\rho}}{4}\right], \tag{17}$$

where erfc is the complementary error function. The limits for high and low particle concentration are given by

$$\mathrm{MFPT} \to \frac{\pi(1+\hat{\gamma})^2}{8\hat{D}\hat{\rho}^2}, \quad \frac{1}{\hat{x}^*_{\mathrm{range}}} \ll \hat{\rho} \ll \frac{1}{\hat{x}^{**}_{\mathrm{range}}},$$
$$\mathrm{MFPT} \to \frac{1}{f\hat{\rho}}, \quad \hat{\rho} \ll \frac{1}{\hat{x}^*_{\mathrm{range}}}, \tag{18}$$

where the high-density limit corresponds to diffusive scaling of MFPT with the distance between particles while the low-density limit corresponds to ballistic scaling. Setting these two limits equal to each other indicates that a transition in the encounter times occurs at a critical length scale

$$\frac{1}{\hat{\rho}_{\mathrm{crit}}} = \frac{\hat{x}^*_{\mathrm{range}}}{2}, \tag{19}$$

which can be equivalently expressed as

$$f\,\mathrm{Pe}\left(\frac{1}{\hat{\rho}}\right) = \frac{8}{\pi(1+\hat{\gamma})^2}. \tag{20}$$

This transition corresponds to a particle density where processive walks begin to dominate the ability to rapidly encounter targets, which occurs when the Péclet number for the distance between particles, multiplied by the fraction of time spent walking, is of order unity.

A calculation of the mean first passage time accurate at all length scales can be carried out by numerical inversion of the Laplace-transformed range function (Sec. II B), and the results are plotted in Fig. 5 for two values of particle density. The black line indicates the transition between behavior dominated by diffusive versus by processive particle motion [Eq. (19)]. Below this line, active transport dominates the motion of the particles and the time to reach the target is insensitive to the passive diffusivity. Above this line, passive diffusion dominates and the target search is insensitive to the fraction of time that the particles spend in processive motion. The parameters relevant to two example biological systems (peroxisome transport in fungal hyphae and vesicle transport in *Aplysia* neurons) are marked with dots.

The parameters for peroxisome transport fall near the transition region, where both passive diffusion and active processive walks contribute to the ability of these organelles to reach any target position within the cell. While previous modeling studies have indicated that both transport mechanisms are important to the maintenance of a uniform distribution of peroxisomes in hyphae [24], we demonstrate here that the particle density falls in an intermediate regime such that diffusion and active walks both contribute to efficient target search by the population

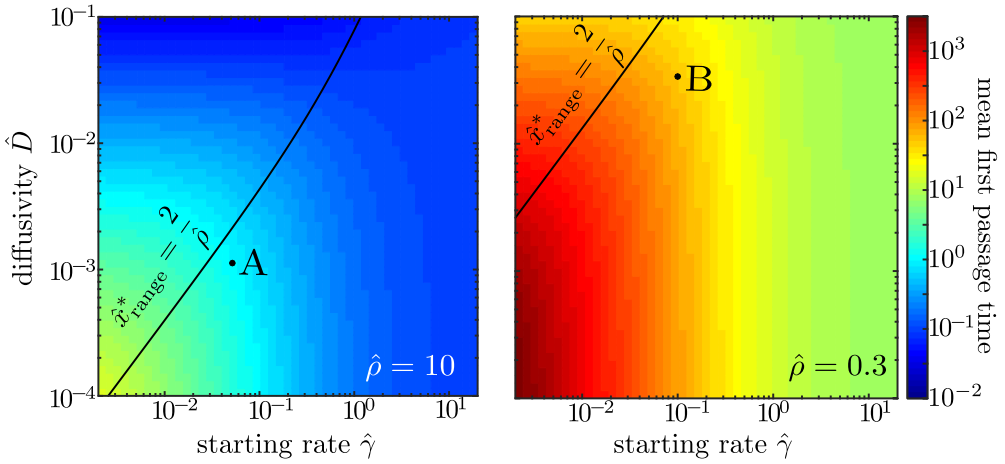

FIG. 5. Average time for target capture by a population of uniformly distributed particles, with two different densities $\hat{\rho} = 10$ (left) and $\hat{\rho} = 0.3$ (right). All units are nondimensionalized by run length ℓ and run time ℓ/v. Marked points show estimated parameters for two cellular systems: *A*, peroxisome transport in fungal hyphae [2], and *B*, vesicle transport in *Aplysia* axons [47] (see Table I). Black lines mark the transition between diffusion-dominated and transport-dominated motion on the length scale of interparticle distance [Eq. (19)].

of peroxisomes. In the case of vesicle transport in *Aplysia* neurons, the lower density of organelles suggests a greater contribution from the active mode as shown in Fig. 5.

We note that for our model with capture occurring in both the active and the passive state, the range over the relevant length scale increases monotonically with the fraction of time spent walking. Hence, the rate of capture is always increased by raising the frequency of starting an active walk $\hat{\gamma}$. This is not the case for particles that can only capture their target in the passive state (see Appendix B), which could include encapsulated proteins that must first exit a vesicle to carry out their function. For such particles, frequent runs decrease the fraction of time spent in a functional state and thus hinder target capture (Fig. 7), an effect that has previously been noted in studies of multimodal search processes [12,19].

V. TRANSPORT IN A TUBE AND THE BENEFITS OF TETHERING

Active transport in a cell occurs via motor proteins attached to microtubule tracks. Even very narrow cellular projections are typically substantially wider than the diameter of a single microtubule. Consequently, organelles must navigate transversely through the cytoplasmic environment in order to encounter a microtubule and engage in active processive motion. A mechanism to keep organelles located close to the microtubule can improve transport efficiency by reducing this search time. In many cases, organelles are believed to be tethered to the microtubule tracks, preventing them from dissociating and diffusing even when they pause after a processive walk. This tethering can be accomplished by additional inactive motors attached to the organelle [37,61] or by specific molecular adaptors linking the organelle directly to the microtubule [39,62].

It has been speculated that tethering can enhance transport by forcing the organelle to remain in proximity to the microtubule tracks, thereby effectively increasing the rate at which processive walks are initiated [7]. At the same time, tethering can severely limit the intracellular space that can be explored by an organelle in the passive state, either by reducing the axial diffusivity in the case where inactive motors slide diffusively along microtubules [37,38] or by halting it entirely in the case of organelle docking [39]. The benefits of tethering thus depend on the relative balance between active and passive transport, as well as the radial size of the domain around the microtubule, which determines the delay associated with encountering the track. The former aspect is dependent on the length scale over which transport must be achieved, as discussed in the previous sections.

We extend our halting creeper model to a three-dimensional cylindrical domain of radius R, wherein active runs can be initiated only within a radius of size $a < R$, corresponding to a small region surrounding a central track. While cellular projections such as hyphae and axons generally have multiple microtubule bundles [24,63], this model serves as an approximation where the size of the cylindrical domain sets the cross-sectional density of the microtubule bundles. In a typical fungal hypha, there are on average two microtubule bundles along the axis [24,64,65]. Assuming the microtubule bundles to be points distributed uniformly on the transverse section of the cylinder, the average distance between two bundles can be calculated as $128r/45\pi$, where r is the radius of the cross section [66]. The domain radius in our model can be considered to be half of this distance, which gives an estimate of $R \approx 0.45\ \mu$m for a typical hyphal diameter of $2\ \mu$m. This is substantially larger than the peroxisome radius (approximately equal to 100 nm) [24], so organelles can only interact with the microtubules over a small fraction of the available cross-sectional area.

In addition to bidirectional walking and passive diffusion states, the particles in this extended model can also enter a tethered state with rate k_b while within the encounter radius a. For simplicity, we assume that particles in the tethered state are entirely immobilized. The model could be extended in a straightforward manner to limited but nonzero diffusivity while in the tethered state. Exit from the tethered state occurs at rate k_u, with the particle unbinding to a uniform radial distribution within the capture radius a. A dimensionless binding strength for tethering is defined by $K_{\mathrm{eq}} = k_b/k_u$.

We note that this model assumes that tethering does not in any way hinder the initiation of an active run, so particles transition to the active state with the same rate regardless of whether they are bound or freely diffusing within the capture radius. While it is possible for tethering to either speed up or slow down the association of an organelle with a motor or a carrier particle, depending on the length, flexibility, and configuration of the tether, we neglect this effect here. Our model for transport in a cylindrical tube around a microtubule track is summarized schematically in Fig. 6(a).

In the limit of rapid transverse diffusivity or small domain size ($D/R^2 \gg \gamma, k_b$), diffusive particles remain equilibrated throughout the cross section of the domain and the effective rates of starting a walk or binding become $\alpha^2\gamma$ and $\alpha^2 k_b$, respectively, where $\alpha = a/R$. In this limit, the delays associated with transverse diffusive transport are eliminated and the equilibrium fraction of particles in each state can be easily calculated (Appendix C). For particles starting at equilibrium, the long-time diffusivity is then given by

$$\begin{aligned}
\hat{D}_{\mathrm{eff}} &= \hat{D} f_{\mathrm{diff}} + f_{\mathrm{walk}}, \\
f_{\mathrm{walk}} &= \frac{\hat{\gamma}\alpha^2}{\hat{\gamma}\alpha^2 + \left(\frac{\alpha^2 K_{\mathrm{eq}} + \hat{\gamma}/\hat{k}_u + 1}{K_{\mathrm{eq}} + \hat{\gamma}/\hat{k}_u + 1}\right)}, \\
f_{\mathrm{diff}} &= \frac{\left(\frac{\hat{\gamma}/\hat{k}_u + 1}{K_{\mathrm{eq}} + \hat{\gamma}/\hat{k}_u + 1}\right)}{\hat{\gamma}\alpha^2 + \left(\frac{\alpha^2 K_{\mathrm{eq}} + \hat{\gamma}/\hat{k}_u + 1}{K_{\mathrm{eq}} + \hat{\gamma}/\hat{k}_u + 1}\right)},
\end{aligned} \tag{21}$$

where f_{walk} and f_{diff} are the fraction of particles in the active and diffusive state, respectively. We again nondimensionalize all length units by the run length ℓ and all time units by the runtime ℓ/v, for consistency with previous calculations.

In the more general case where the delay due to transverse diffusion is included, it can be shown (see Appendix D) that for a particle which begins uniformly distributed in the diffusive state within radius a, the mean waiting time to enter a walking state is identical to the fast-diffusion limit and is given by

$$\langle \hat{t}_w \rangle = \frac{1}{\hat{\gamma}} \left[\frac{\alpha^2 K_{\mathrm{eq}} + 1 + \hat{\gamma}/\hat{k}_u}{\alpha^2 (K_{\mathrm{eq}} + 1 + \hat{\gamma}/\hat{k}_u)} \right]. \tag{22}$$

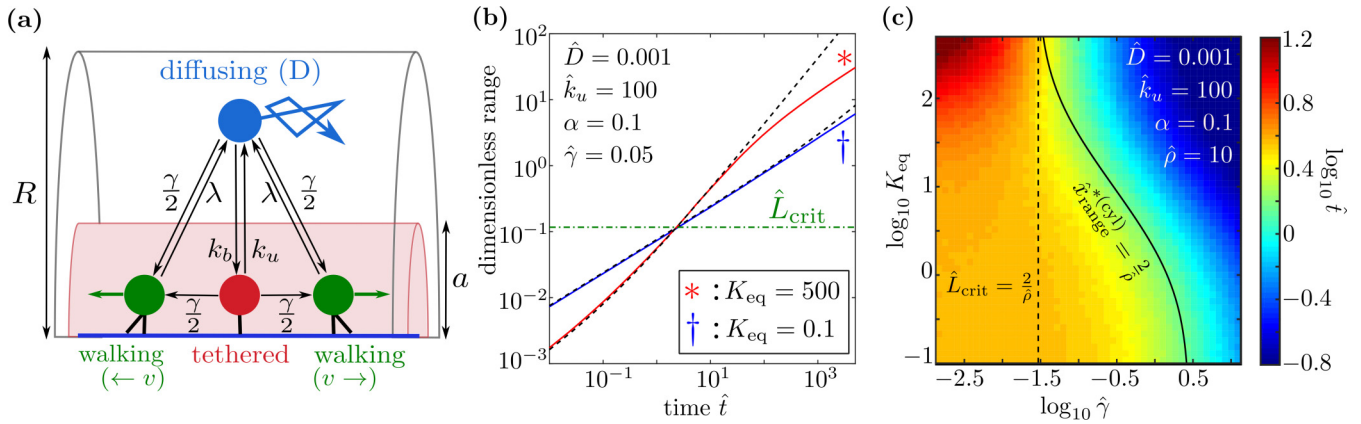

FIG. 6. Effects of tethering on transport. (a) Schematic for the tethering model. The smaller cylinder denotes the region within which particles can tether to the microtubule or initiate active transport. The transition rates between states are indicated with the arrows. (b) Range vs time for weak ($K_{eq} = 0.1$) and strong ($K_{eq} = 500$) tethering. Dashed black lines show analytical approximations in the limits of no tethering and infinitely strong tethering, accurate for short to intermediate times [Eq. (24)]. The horizontal dash-dotted line indicates the transition length scale $\hat{L}_{crit}$ where tethering becomes advantageous. (c) Average time for target capture by a population as a function of the starting rate $\hat{\gamma}$ and binding strength K_{eq}. The solid line indicates the transition from diffusive to active transport as the dominant transport mode at different values of tethering strength. The dashed line shows the transition where strong tethering becomes advantageous for the target encounter.

This average time ranges from $1/\alpha^2\gamma$ in the limit of low binding strength to $1/\gamma$ in the limit of strong binding and is independent of the diffusivity D. In the case of very slow diffusion, those particles that escape the binding radius a take a long time to return, but such escape before initiating a walk becomes concomitantly less likely, with these two effects canceling each other out in the calculation of the average time to start walking. Because particles are assumed to distribute uniformly across radius a when leaving the tethered state, this equivalence of the average time to initiate a subsequent walk means that the long-time behavior of particles matches the fast-diffusivity limit, regardless of the actual value of D.

By contrast, we note that the standard deviation in the time required to start a walk, for a particle that starts diffusive and uniformly distributed within a, is dependent on the diffusivity (see Appendix D). Slow diffusion and strong binding can greatly increase the variance in the time required for a particle to start a walk, leading to large variability in the amount of time individual particles remain in a passive or tethered state over a particular time interval of observation. This extreme case may contribute to the identification of apparently immobile populations of particles observed in some *in vivo* organelle tracking studies [25].

The effectiveness of tethering in improving transport over a long time can be inferred from the derivative of the effective diffusivity $\hat{D}_{eff}$ with respect to the binding strength K_{eq}. A positive derivative signifies that long-range transport is accelerated by tethering, whereas a negative value indicates that tethering hinders transport. Tethering is advantageous in the long-time limit when the following criterion is satisfied:

$$(1-\alpha^2)\left(\frac{\hat{\gamma}}{\hat{\gamma}+1}\right)\mathrm{Pe}(\ell) > 1. \tag{23}$$

This expression summarizes the idea that tethering is helpful for long-range transport in situations where the domain is wide ($\alpha^2 \ll 1$), where the rate of walking is substantial compared to the pausing rate ($\hat{\gamma} \gg 1$) and where active runs move the particles faster than diffusion over the longest processive length scale [$\mathrm{Pe}(\ell) \gg 1$].

Below the long-time diffusive limit, the extent to which tethering aids transport depends on the length scale of interest. In particular, at times much shorter than the cycle time to initiate and stop an active walk, the dimensionless particle range can be approximated by

$$Z(\hat{t}) \approx 4 f_{diff}\sqrt{\frac{\hat{D}\hat{t}}{\pi}} + f_{walk}\hat{t}, \tag{24}$$

in a manner analogous to Eq. (8). This expression can be inverted to calculate the time at which a particular range is reached. Comparing the low-K_{eq} and high-K_{eq} limits indicates that the ability of particles to tether to the track allows them to explore more rapidly over length scales above

$$\hat{L}_{crit} = x^*_{range}\frac{(1+\hat{\gamma})^2}{(1-\alpha^2)^2}. \tag{25}$$

For large domains ($\alpha \ll 1$) and low propensity for active walking ($\hat{\gamma} \ll 1$), tethering is helpful over all length scales where processive active motion is the dominant form of transport, as defined by the critical length $\hat{x}^*_{range}$ [Eq. (10)].

We use kinetic Monte Carlo methods to simulate the spreading of particles within our cylindrical model. The simulations are accelerated with the use of analytically calculated Green's functions to propagate the particles within homogeneous cylindrical domains (see Appendix E), allowing for efficient sampling of particle behavior over a broad set of parameters.

The average axial range for a population of particles can be obtained as a function of time from the simulations. Figure 6(b) shows the time evolution of the range for weak and strong tethering. The transport parameters used are relevant for peroxisomes in fungal hyphae (Table I), with the domain width assumed to be $R = 1\ \mu$m and a central region of width $a = 0.1\ \mu$m. For consistency with previous calculations, results are reported in dimensionless units, using the run length ($\ell \approx 7\ \mu$m) and processive walking time ($1/\lambda \approx 3$ s) as the

length and time units. The critical length scale for this system is $\hat{L}_{\text{crit}} \approx 0.12$, below which the average range for strongly tethered particles is lower than the weakly tethered ones. For length scales above $\hat{L}_{\text{crit}}$, strongly tethered particles explore over a greater range. The full extent of a hyphal growth tip ($\hat{L} \approx 8$) is several times longer than this critical length scale, highlighting the potential benefit of tethering for distributing peroxisome particles over the entire growth tip.

Having established the length scales over which tethering is advantageous, we now calculate explicitly the effect of tethering on the average search time by a population of particles with dimensionless density $\hat{\rho}$. The capture time is defined as the first passage time to an arbitrary cross section of the cylinder, by a population of particles equilibrated between states and uniformly distributed along the axis of the cylinder. We note that in the case of a target that is located off the central axis where active motion and tethering take place, this target could only be reached if the particle passes through the appropriate axial location in the passively diffusing state. The capture time should then be calculated using the distribution of first passive passage times, as discussed in Appendix B. In the limit of very rapid transverse diffusivity, capture times for an off-axis target could be derived directly from the first passive passage to a cross section. For slow transverse diffusivity, multiple passages through the cross section in the passive state would be required to hit a target that is much smaller than the cross-sectional area. Because the relationship between particle range and first passage times [Eq. (16)] breaks down in the case where only passive passage is considered, extracting target capture times in our full three-dimensional model would require direct simulation of first passage by individual particles. While this case would make a promising extension for future work, for the sake of simplicity we focus here on targets localized at the central axis.

A surface plot of the average capture times versus binding strength K_{eq} and walking rate $\hat{\gamma}$ is shown in Fig. 6(c). The effect of tethering on the average time to target capture varies depending on $\hat{\gamma}$. For particles with a very small probability of engaging in active runs, tethering hinders target search by limiting mobility in the passive state. For particles with a high propensity for active motion, tethering can aid their ability to encounter targets by increasing the amount of time spent in the region where active runs can be initiated. We approximate the parameter regime where this transition occurs by analytically calculating the integral for the MFPT [Eq. (16)], using the short-time approximation of the particle range [Eq. (24)]. Comparing the low-K_{eq} and high-K_{eq} limits yields a transition at a critical particle density

$$\hat{\rho}_{\text{tether}} = \left(\frac{2}{\hat{L}_{\text{crit}}}\right)\left(\frac{1+\alpha^2\hat{\gamma}}{1-\alpha^2}\right)^2. \tag{26}$$

For small values of α and $\hat{\gamma}$, this transition is equivalent in form to the critical length scale where processive walks first begin to play an important role, as calculated in Eq. (19). For parameters relevant to the motion of peroxisomes in fungal hyphae, we compare the critical particle density ($\hat{\rho}_{\text{tether}} \approx 17$) with the observed density of peroxisomes ($\hat{\rho} \approx 10$). Because the observed density is comparable to the critical density, we expect that tethering would not substantially hinder the ability of the peroxisomes to patrol the cytoplasm and encounter targets within the cell.

For a given finite binding strength K_{eq}, the MFPT to the target will be dominated by either diffusive or processive motion, depending on the fraction of particles in each state. The transition to the regime where encounter times are sensitive to the initiation of active walks occurs when the spacing between particles hits a critical length scale where such walks between to dominate. This length can be obtained analogously to the expression for $\hat{x}^*_{\text{range}}$ [Eq. (10)] by replacing the starting rate $\hat{\gamma}$ with an effective starting rate based on the average time to initiate a walk: $\hat{\gamma}_{\text{eff}} = 1/\langle t_w \rangle$. In the case of rapid binding or unbinding ($\hat{k}_u \gg \hat{\gamma}$), this rate is approximated as

$$\hat{\gamma}_{\text{eff}} \approx \hat{\gamma}\left[\frac{\alpha^2(K_{\text{eq}}+1)}{\alpha^2 K_{\text{eq}}+1}\right]. \tag{27}$$

The critical particle density is then given by

$$\hat{\rho}^{(\text{cyl})}_{\text{crit}} = \frac{2}{\hat{x}^{*(\text{cyl})}_{\text{range}}} = \frac{\pi\hat{\gamma}_{\text{eff}}}{8\hat{D}}, \tag{28}$$

where $\hat{x}^{*(\text{cyl})}_{\text{range}}$ is the length scale for transition between diffusive and processive motion in the model of a halting creeper within a cylindrical domain. This transition is shown with a solid black line in Fig. 6(c).

VI. SUMMARY

We have employed a simplified halting creeper model, consisting of stochastic interchange between passive diffusion and active processive walks, to investigate the efficiency of transport within an extended cylindrical domain. Specifically, this model is applicable to the transport of organelles within long narrow cellular processes such as neural axons and fungal hyphae. We explored the space of relevant parameters, including the rates of transition between passive and active states and the relative speed of diffusion versus active transport, as characterized by the Péclet number over different length scales. Our results highlight the importance of the relevant length scale in determining the contributions of the different transport modes and we identified simple expressions for the time ($t^*_{\text{range}} = \frac{16D\lambda^2}{\pi v^2\gamma^2}$) and length [$x^*_{\text{range}} = \frac{16D\lambda^2}{\pi v\gamma(\lambda+\gamma)}$] at which processive motion dominates particle spreading. We emphasized the use of the average range as a metric for the ability of particles to explore their domain via multimodal transport, demonstrating that passive diffusion can play an important role over longer length scales than expected based on the classic analysis of the mean square displacement.

We focused specifically on the contributions of active and passive transport to several key objectives relevant to the cell. First, we considered the establishment of a uniform distribution from a bolus of particles, demonstrating that efficient dispersion is achieved at intermediate run lengths that can be substantially smaller than the domain size. This result indicates the importance of bidirectional active transport with frequent reversals in the movement of particles that must be spread broadly throughout a large domain, as is the case with metabolic organelles such as peroxisomes and mitochondria. Second, we quantified the rate at which a single particle first encounters a stationary target, showing again an advantage

to intermediate run lengths that minimize the time wasted pursuing a long processive walk in the wrong direction. Third, we considered the rate of encounter to a target by the first of a population of halting creeper particles, identifying the parameter regime where active transport or diffusion dominate the motion, and showing that examples of biological interest fall in the intermediate regime where both modes of transport contribute substantially to target encounter.

Finally, we investigated an extension of the one-dimensional model to a cylindrical domain, where active transport can only occur in a narrow region along the axis and where particles can enter a halted tethered state that both enhances the effective rate of initiating an active run and limits their ability to explore the domain while in the passive state. The advantages of tethering to microtubule tracks have been a topic of much speculation in the literature on intracellular transport [7,37,38]. We delineated the parameter regime in which tethering is expected to aid the long-time dispersion of particles [Eq. (23)] and identified a critical length scale L_{crit} [Eq. (25)] below which tethering hinders the ability of the particles to explore their domain. For several example intracellular transport systems (Table I), this critical length is on the order of a few hundred nanometers, confirming the advantages of tethering for transport over micron length scales.

The results derived in this work highlight the complementary role of diffusion and processive transport in fulfilling cellular goals for delivering and distributing cytoplasmic organelles. The derived expressions can be employed for analyzing data on measured transport parameters to determine the length scales and transport objectives where active motor-driven motion is expected to dominate, where bidirectional transport with limited processivity is advantageous, and where tethering to cytoskeletal tracks can aid overall organelle dispersion.

ACKNOWLEDGMENTS

We thank A. Agrawal and C. Niman for helpful comments on the manuscript and S. Reck-Peterson for fruitful discussions.

APPENDIX A: PROPAGATOR FOR A ONE-DIMENSIONAL HALTING CREEPER

We calculate the position distribution of a particle switching between diffusive transport with diffusivity D and processive motion with speed v. Switching between states is a Poisson process with rate γ for entering an active state and rate λ for leaving an active state (see Fig. 1). The overall spatial distribution can be obtained by a convolution of propagators for individual states, summed over all possible state transitions.

Starting at an initial position $x = 0$, the spatial distribution of a diffusive particle at a time t is

$$R_D(x,t) = \frac{1}{\sqrt{4\pi Dt}} e^{-x^2/4Dt}. \tag{A1}$$

We define the joint distribution that the particle first switches to an active state at time t while at position x by

$$H_D(x,t) = \gamma e^{-\gamma t} R_D(x,t). \tag{A2}$$

A Fourier transform in space ($x \to k$), followed by a Laplace transform in time ($t \to s$), gives

$$\hat{\tilde{H}}_D(k,s) = \frac{\gamma}{(\gamma + Dk^2 + s)}. \tag{A3}$$

The position distribution of particles starting at $x = 0$ in the active state, moving with a velocity v at time t, is given by

$$R_{\pm}(x,t) = \delta(x \mp vt). \tag{A4}$$

The corresponding joint distribution for the time and location of switching from the active to the passive state is

$$H_{\pm}(x,t) = \lambda e^{-\lambda t} \delta(x \mp vt). \tag{A5}$$

The Fourier- and Laplace-transformed distribution is given by

$$\hat{\tilde{H}}_{\pm}(k,s) = \frac{\lambda}{(\lambda + s \mp \mathrm{i}kv)}. \tag{A6}$$

We define a step in the particle's trajectory as a switch from the passive to the active state and back to the passive state again. If the particle starts in the passive state at zero time, the position and time distribution at the end of one such step can be expressed as

$$M(x,t) = \int_{-\infty}^{\infty} dx' \int_0^t dt' H_D(x',t') \times \left[\frac{H_+(x-x',t-t') + H_-(x-x',t-t')}{2} \right], \tag{A7}$$

where the first term denotes a particle reaching x' at time t' via diffusion and the second term denotes the particle covering a distance $x - x'$ in the remaining time $t - t'$ by walking, integrated over all values of x' and t'. The Fourier- and Laplace-transformed function for the propagation of the particle after a full step of active and passive motion is given by

$$\hat{\tilde{M}}(k,s) = \hat{\tilde{H}}_D(k,s) \left(\frac{\hat{\tilde{H}}_+(k,s) + \hat{\tilde{H}}_-(k,s)}{2} \right). \tag{A8}$$

To get the spatial propagator of a halting creeper particle that both starts and ends in a passive state, we sum over all possible paths between the active and passive states, convolved with the probability that the particle does not leave the passive state in the final time interval [given by $H_D(x,t)/\gamma$]. The resulting expression for the propagator can then be expressed as

$$G_{DD}(x,t) = \frac{H_D}{\gamma} + M *_{x,t} \left(\frac{H_D}{\gamma} \right) + M *_{x,t} M *_{x,t} \left(\frac{H_D}{\gamma} \right) + \cdots, \tag{A9}$$

where $*_{x,t}$ denotes convolution with respect to x and t. The first term in the summation corresponds to a particle that never left the passive state, the second term to a particle that performs a single active step before returning to the passive state, the third term includes two active steps, and so forth. Applying a Fourier transform in space and a Laplace transform in time

transforms the convolutions into a geometric series, leading to

$$\hat{\tilde{G}}_{DD}(k,s) = \frac{\left(\frac{\hat{\tilde{H}}_D(k,s)}{\gamma}\right)}{1-\hat{\tilde{M}}(k,s)} = \frac{(s+\lambda)^2+k^2v^2}{(s+\gamma+Dk^2)[(s+\lambda)^2+k^2v^2]-\gamma\lambda(s+\lambda)}, \tag{A10}$$

where the second line follows by substituting expressions from Eqs. (A3) and (A8).

The distributions for the other quantities appearing in Eqs. (5) and (6) can be derived similarly. The transformed distributions are

$$\begin{aligned}
\hat{\tilde{G}}_{DW} &= \frac{\gamma(s+\lambda)}{(s+\gamma+Dk^2)[(s+\lambda)^2+k^2v^2]-\gamma\lambda(s+\lambda)},\\
\hat{\tilde{G}}_{WW} &= \frac{(s+\gamma+Dk^2)(s+\lambda)}{(s+\gamma+Dk^2)[(s+\lambda)^2+k^2v^2]-\gamma\lambda(s+\lambda)},\\
\hat{\tilde{G}}_{WD} &= \frac{\lambda(s+\lambda)}{(s+\gamma+Dk^2)[(s+\lambda)^2+k^2v^2]-\gamma\lambda(s+\lambda)},\\
\hat{\tilde{G}}_{\pm D} &= \frac{\lambda(s+\lambda\pm ikv)}{(s+\gamma+Dk^2)[(s+\lambda)^2+k^2v^2]-\gamma\lambda(s+\lambda)},\\
\hat{\tilde{G}}_{\pm W} &= \frac{(s+\gamma+Dk^2)(s+\lambda\pm ikv)}{(s+\gamma+Dk^2)[(s+\lambda)^2+k^2v^2]-\gamma\lambda(s+\lambda)}.
\end{aligned} \tag{A11}$$

A linear combination of these distributions, weighted by the equilibrium fraction of particles in each state, is used to derive the overall propagator in Eq. (1):

$$\hat{\tilde{G}} = \frac{\gamma}{\gamma+\lambda}(\hat{\tilde{G}}_{WD}+\hat{\tilde{G}}_{WW}) + \frac{\lambda}{\gamma+\lambda}(\hat{\tilde{G}}_{DD}+\hat{\tilde{G}}_{DW}). \tag{A12}$$

The expressions obtained can be transformed back to real space and real time by a combination of analytical and numerical methods. To calculate the Laplace-transformed expressions (5)–(7) we invert the Fourier transform analytically as $\hat{G}(x,s) = \frac{1}{2\pi}\int_{-\infty}^{\infty} e^{ikx}\hat{\tilde{G}}(k,s)dk$. The Laplace transform of the range and first passage time distribution can then be inverted numerically using Talbot's algorithm [52].

APPENDIX B: FIRST PASSIVE PASSAGE TIME

For certain intracellular particles such as mRNAs [67] and proteins encapsulated within transport vesicles, we would expect that the particles are unable to perform their target-capture functions while in the processively moving state. Under this restriction, it is desirable to know how much time is required for an organelle to reach its target in the correct state while undergoing multimodal transport. An important quantity in this context is the passive first passage time distribution $F_P(x,t)$, which is the overall probability density for the time t at which the particle first passes position x in a diffusive state. While the renewal equations (5) and (6) can be used to obtain the probability of first passage occurring in the diffusive state, in order to obtain the required distribution we must also consider particles that achieve first passage in the processive state and after subsequent state transitions eventually return to the target in the diffusive state.

The halting creeper model allows for the calculation of $F_P(x,t)$ by summing over all trajectories that first pass the target in the diffusive state at the specified time. For particles that pass in the processive state, the turning events required to return to the target can be expressed as a series of convolutions over time. A Laplace transform $F_P(x,t) \to \hat{F}_P(x,s)$ converts these convolutions to multiplication, leading to an expression for the first passive passage time distribution

$$\begin{aligned}
\hat{F}_P(x,s) = \hat{F}_{*D}(x,s) &+ \hat{F}_{*+}(x,s)\\
&\times [\hat{F}_{+D}(0^-,s) + \hat{F}_{+-}(0^-,s)\hat{F}_{-D}(0^+,s)]\\
&\times \sum_{m=0}^{\infty}[\hat{F}_{+-}(0^-,s)\hat{F}_{-+}(0^+,s)]^m,
\end{aligned} \tag{B1}$$

where $\hat{F}_{ij}(x,s)$ denotes the Laplace-transformed first passage time distribution of a particle starting in the state i and reaching the target position x in the state j. The possible states are the passive state (D), walking in the forward or backward direction ($\pm$), and walking in any direction (W). An asterisk denotes a sum over all possible starting states, weighted by the respective steady-state probabilities for each state. The first term in the expression denotes the particles that reach the target in the diffusive state for the first time. Subsequent terms in the infinite sum include particles which need to change states and return to the target position, with each term denoting an additional return to the target in a nonfunctional state.

Under the assumption of symmetric starting rates, we can write $\hat{F}_{+-}(0^-,s) = \hat{F}_{-+}(0^+,s)$ and $\hat{F}_{+D}(0^-,s) = \hat{F}_{-D}(0^+,s)$, which reduces Eq. (B1) to

$$\hat{F}_P(x,s) = \hat{F}_{*D}(x,s) + \frac{\hat{F}_{*+}(x,s)\hat{F}_{-D}(0^+,s)}{1-\hat{F}_{-+}(0^+,s)}. \tag{B2}$$

Equations (5) and (6) allow us to calculate the probability density of a particle that starts at equilibrium executing first passage at a particular time while in the passive state [$\hat{F}_{*D}(x,s)$] or while actively walking forward [$\hat{F}_{*+}(x,s)$]. Other quantities appearing in Eq. (B2) can be calculated from the renewal equations for particles starting in the active state walking backward,

$$\begin{aligned}
G_{-D}(x;t) &= \int_0^t dt'[F_{-D}(t';x)G_{DD}(0;t-t')\\
&\quad + F_{-+}(t';x)G_{+D}(0;t-t')],\\
G_{-W}(x;t) &= \int_0^t dt'[F_{-D}(t';x)G_{DW}(0;t-t')\\
&\quad + F_{-+}(t';x)G_{+W}(0^+;t-t')].
\end{aligned} \tag{B3}$$

After a Laplace transform, Eq. (B3) reduces to a system of linear equations

$$\begin{bmatrix}\hat{G}_{DD}(0) & \hat{G}_{+D}(0)\\ \hat{G}_{DW}(0) & \hat{G}_{+W}(0^+)\end{bmatrix}\begin{bmatrix}\hat{F}_{-D}(x)\\ \hat{F}_{-+}(x)\end{bmatrix} = \begin{bmatrix}\hat{G}_{-D}(x)\\ \hat{G}_{-W}(x)\end{bmatrix}, \tag{B4}$$

where the argument $t \to s$ is implied. The right-hand side can be evaluated at $x = 0^+$ by carrying out the Fourier inversion of $\hat{\tilde{G}}_{-D}$ and $\hat{\tilde{G}}_{-W}$ through direct integration of the expressions (A11) over k. The Laplace-transformed first passive passage

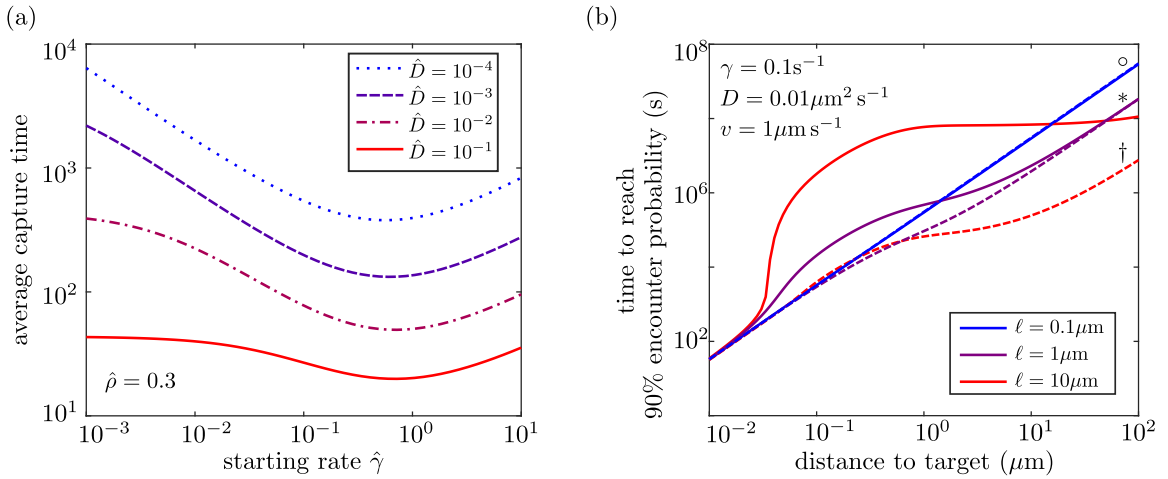

FIG. 7. Effects of state-dependent activity: (a) Time to reach 90% capture probability $t_{90\%}$ for different run lengths and biologically relevant transport parameter values. Solid lines denote $t_{90\%}$ for particles that can capture their target only in the passive state. Dashed lines denote $t_{90\%}$ for particles that capture their target in either state. The $\circ$, $*$, and $\dagger$ denote run lengths of 0.1, 1, and 10 μm, respectively. Plots for $\ell = 0.1$ μm overlap. (b) Average time for target capture by a uniformly distributed population as a function of the starting rate $\hat{\gamma}$ for different values of diffusivity $\hat{D}$. The particle density $\hat{\rho} = 0.3$ and other parameter ranges include the observed parameters for peroxisome transport in fungal hyphae.

time distributions $\hat{F}_{-D}$ and $\hat{F}_{-+}$ are then inverted numerically using Talbot's algorithm [52].

We study the implications of this search process, where particles are functional only in the passive state, by first calculating the time required for a single particle to reach its target with 90% probability [Fig. 7(a)]. As in the case where both active and passive states allow capture, we see that an intermediate run length can optimize the capture time. However, when only passive capture is allowed, this optimal run length is shifted to much shorter values, as would be expected since long run lengths result in the particle spending less time in a functional state.

Additionally, we calculate the average time required by any particle within a uniformly distributed population (of density $\hat{\rho} = 0.3$) to reach a stationary target [Fig. 7(b)]. As compared to a particle that is functional in both states (Fig. 5), the diffusivity has a much bigger role to play for a particle that can only capture while passive. Because increasing diffusivity allows a particle to search a wider region during each sojourn in a functional state, the diffusion coefficient substantially modulates the capture time even at very large values of $\hat{\gamma}$. Furthermore, in the case of passive capture, increasing the fraction of processively moving particles does not necessarily speed up capture. An optimum starting rate $\hat{\gamma}$ arises from two competing effects. On the one hand, the faster transport in the processive state allows particles to reach the region near the target more rapidly. On the other hand, a large value of the starting rate proves detrimental, as particles reaching the target are less likely to be in the functional state. This optimization in terms of the fraction of time spent moving processively has previously been noted by several studies on two-dimensional multimodal search processes [12,19,68].

A search process where the particle is functional only in the passive state is applicable to components, such as neurotransmitters, that are encapsulated within vesicles but must be released in order to carry out their function. Additionally, in the case of a tubular cell region (see Sec. V), a target that is located away from the microtubule track could only be reached when the organelle is in the diffusive state.

APPENDIX C: EQUILIBRIUM FRACTION OF PARTICLES

For narrow tubular cells or a rapid transverse diffusivity ($D/R^2 \gg \gamma, k_b$), binding and walking events take much longer than the time required for particles to equilibrate throughout the cross section. In this limit, the effective rates of starting a walk or binding to a tether become $\alpha^2\gamma$ and $\alpha^2 k_b$, respectively, where $\alpha = a/R$. The governing equations for the fraction of particles in each state are then given by

$$\begin{aligned}
\frac{df_{\text{walk}}}{dt} &= \gamma f_{\text{bound}} + \alpha^2\gamma f_{\text{diff}} - \lambda f_{\text{walk}},\\
\frac{df_{\text{bound}}}{dt} &= \alpha^2 k_b f_{\text{diff}} - (k_u + \gamma) f_{\text{bound}},\\
\frac{df_{\text{diff}}}{dt} &= k_u f_{\text{bound}} + \lambda f_{\text{walk}} - \alpha^2(k_b + \gamma) f_{\text{diff}},\\
f_{\text{diff}} + f_{\text{walk}} + f_{\text{bound}} &= 1.
\end{aligned} \tag{C1}$$

The time derivatives vanish in the steady state, reducing Eq. (C1) to a system of linear equations which can be solved to obtain

$$\begin{aligned}
f_{\text{walk}} &= \frac{\gamma\alpha^2}{\gamma\alpha^2 + \lambda\left(\frac{\alpha^2 k_b + \gamma + k_u}{k_b + \gamma + k_u}\right)},\\
f_{\text{diff}} &= \frac{\lambda\left(\frac{\gamma + k_u}{k_b + \gamma + k_u}\right)}{\gamma\alpha^2 + \lambda\left(\frac{\alpha^2 k_b + \gamma + k_u}{k_b + \gamma + k_u}\right)},\\
f_{\text{bound}} &= \frac{\lambda\left(\frac{\alpha^2 k_b}{k_b + \gamma + k_u}\right)}{\gamma\alpha^2 + \lambda\left(\frac{\alpha^2 k_b + \gamma + k_u}{k_b + \gamma + k_u}\right)}.
\end{aligned} \tag{C2}$$

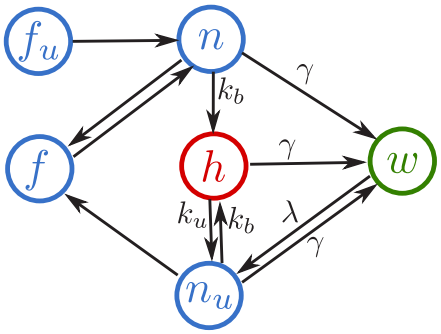

FIG. 8. Schematic state diagram illustrating the particle states used to develop the analytical model for multimodal transport in a cylinder. Allowed transitions are labeled with arrows and the rates for the constant-rate transition processes (to and from the tethered or actively walking state) are indicated. The transitions between diffusive states occur with a time-varying rate that can be derived by evaluating the matrix components in Eq. (D2) at $k = 0$.

APPENDIX D: ANALYTICAL MODEL FOR MULTIMODAL TRANSPORT IN A CYLINDER, WITH TETHERING

In this Appendix we develop the full analytical model for axial transport in a cylinder of radius $R = 1$ for particles capable of passive diffusion with diffusivity D, of initiating active processive walks with a rate γ while within a region of radius α of the central axis, and of entering a stationary tethered state with binding rate k_b while in the same region. The rate constant for unbinding from a tethered state is k_u and for transitioning between an active walk and passive diffusion is λ [see Fig. 6(a) for illustration of the model]. For ease of the derivation, all length units in this Appendix as well as Appendix E are nondimensionalized by the cylinder radius R and all time units are nondimensionalized by R/v, where v is the processive velocity of actively walking particles. We give our final results in fully dimensional units to facilitate comparison with other sections of the paper.

Our model is developed in a manner analogous to the approach previously used for modeling facilitated diffusion by DNA-binding proteins that occurs via a combination of three-dimensional diffusion and one-dimensional sliding along a filament [69]. We describe the particle motion by a system of individual states with Markovian transitions between them. The rates of transition between the states are time varying, depending specifically on the time interval since the particle first entered the state. These states (Fig. 8) consist of a tethered state h, a walking state w, a state n wherein the particle started at radius $\alpha - \epsilon$ and has remained within a radius α, a state n_u where the particle started uniformly distributed within radius α and has remained within that inner region, a state f where the particle started at radius $\alpha + \epsilon$ and has remained outside the inner region at a radius greater than α, and a state f_u where the particle started uniformly distributed in the outer region and has remained in the outer region. When computing statistics for the overall motion of the particle, we take the limit $\epsilon \to 0$. The axial propagation of a particle in states n, n_u, f, and f_u is given by the propagator function for diffusive motion $R_D(x,t)$ [Eq. (A1)]. The axial propagation in state w is given by $\frac{1}{2}[R_+(x,t) + R_-(x,t)]$ [Eq. (A4)].

We construct a transition matrix of propagators $\mathbf{H}$, where $H_{a,b}(x,t)$ is the joint probability density for the time and position of a particle initially at the origin in state a making its first transition out of that state, into state b. A Fourier transform in space $x \to k$ and a Laplace transform in time $t \to s$ is carried out to yield the transformed propagator $\hat{\tilde{\mathbf{H}}}(k,s)$. The components of this propagator matrix are derived from the Laplace-transformed solutions for first passage times to an inner or outer absorbing boundary for a particle diffusing in a cylindrical domain [70]. For instance, the transition propagator from the n state to the f state is given by

$$\begin{aligned} H_{nf}(x,t) &= e^{-(k_b+\gamma)t} J_{nf}(t) R_D(x,t), \\ \tilde{H}_{nf}(k,t) &= e^{-(k_b+\gamma-Dk^2)t} J_{nf}(t), \\ \hat{\tilde{H}}_{nf}(k,s) &= \hat{J}_{nf}(s + k_b + \gamma + Dk^2), \end{aligned} \tag{D1}$$

where $J(t)$ is the distribution of times for a diffusive particle starting at radius $\alpha - \epsilon$ to exit to an absorbing cylindrical boundary at radius α. The full matrix of components is listed below:

$$\begin{aligned} \hat{\tilde{H}}_{f_u,n} &= \frac{2\alpha}{(1-\alpha^2)\sigma_D} \frac{I_1(\sigma_D)K_1(\alpha\sigma_D) - I_1(\alpha\sigma_D)K_1(\sigma_D)}{I_0(\alpha\sigma_D)K_1(\sigma_D) + K_0(\alpha\sigma_D)I_1(\sigma_D)}, \\ \hat{\tilde{H}}_{f,n} &= \frac{I_0[(\alpha+\epsilon)\sigma_D]K_1(\sigma_D) + K_0[(\alpha+\epsilon)\sigma_D]I_1(\sigma_D)}{I_0(\alpha\sigma_D)K_1(\sigma_D) + K_0(\alpha\sigma_D)I_1(\sigma_D)}, \\ \hat{\tilde{H}}_{n_u,f} &= \frac{2}{\alpha\sigma_b} \frac{I_1(\alpha\sigma_b)}{I_0(\alpha\sigma_b)}, \quad \hat{\tilde{H}}_{n,f} = \frac{I_0[(\alpha-\epsilon)\sigma_b]}{I_0(\alpha\sigma_b)}, \\ \hat{\tilde{H}}_{n_u,w} &= \frac{\gamma}{D\sigma_b^2}(1 - \hat{\tilde{H}}_{n_u,f}), \quad \hat{\tilde{H}}_{n,w} = \frac{\gamma}{D\sigma_b^2}(1 - \hat{\tilde{H}}_{n,f}), \\ \hat{\tilde{H}}_{n_u,h} &= \frac{k_b}{D\sigma_b^2}(1 - \hat{\tilde{H}}_{n_u,f}), \quad \hat{\tilde{H}}_{n,h} = \frac{k_b}{D\sigma_b^2}(1 - \hat{\tilde{H}}_{n,f}), \\ \hat{\tilde{H}}_{h,w} &= \frac{\gamma}{s+\gamma+k_u}, \quad \hat{\tilde{H}}_{h,n_u} = \frac{k_u}{s+\gamma+k_u}, \\ \hat{\tilde{H}}_{w,n_u} &= \frac{\lambda(s+\lambda)}{(s+\lambda)^2 + k^2}, \end{aligned} \tag{D2}$$

where $\sigma_D = \sqrt{(s+Dk^2)/D}$, $\sigma_b = \sqrt{(s+\gamma+k_b+Dk^2)/D}$, and I_ν and K_ν are the modified Bessel functions of order ν of the first and the second kind, respectively. All other components of $\hat{\tilde{\mathbf{H}}}$ not listed in Eq. (D2) correspond to transitions not allowed in the model and are equal to 0. To calculate the overall distribution of particles, we additionally define a vector of propagators $\hat{\tilde{\mathbf{F}}}$. Each component $\hat{\tilde{F}}_a$ corresponds to the Fourier-Laplace-transformed spatial distribution of particles that first reached state a at time 0 and have moved a displacement x at time t, without having left that state. These components can be expressed in terms of the transition propagators $H_{a,b}$ by calculating the overall probability that the particle has not left its current state. For instance,

$$\begin{aligned} F_n(x,t) &= \left[1 - \int_0^t J_{nf}(t')dt'\right] e^{-(k_b+\gamma)t} R_D(x,t), \\ \hat{\tilde{F}}_n(k,s) &= \frac{1}{s + Dk^2 + k_b + \gamma}[1 - \hat{\tilde{J}}_{nf}(k, s + Dk^2 + k_b + \gamma)] \\ &= \frac{1}{s + Dk^2 + k_b + \gamma}(1 - \hat{\tilde{H}}_{nf}). \end{aligned} \tag{D3}$$

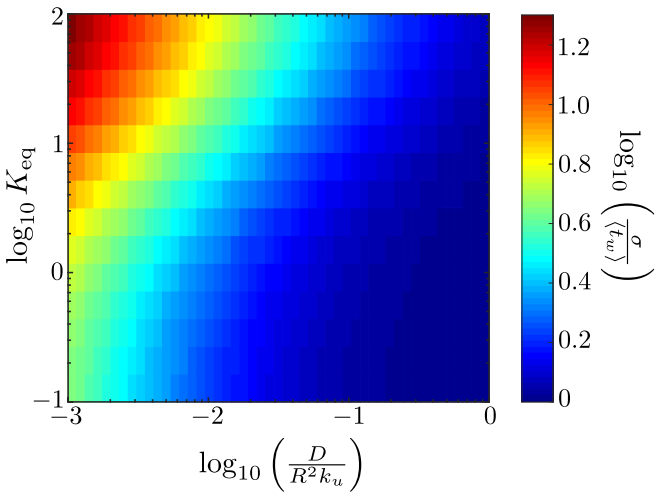

FIG. 9. Fano factor $\sigma/\langle t_w\rangle$ quantifying the variability in the time required for a particle to first begin a processive walk. The particle is assumed to start uniformly distributed within the inner radius α. Results shown are for the parameters $\alpha = 0.1$, $k_u = 100$, and $\gamma = 10^{-2}$.

The other components can be derived analogously, to give

$$\hat{\tilde{F}}_{f_u} = \frac{1}{D\sigma_D^2}(1-\hat{\tilde{H}}_{f_u,n}), \quad \hat{\tilde{F}}_f = \frac{1}{D\sigma_D^2}(1-\hat{\tilde{H}}_{f,n}),$$
$$\hat{\tilde{F}}_{n_u} = \frac{1}{D\sigma_b^2}(1-\hat{\tilde{H}}_{n_u,f}), \quad \hat{\tilde{F}}_n = \frac{1}{D\sigma_b^2}(1-\hat{\tilde{H}}_{n,f}),$$
$$\hat{\tilde{F}}_w = \frac{s+\lambda}{(s+\lambda)^2+k^2}, \quad \hat{\tilde{F}}_h = \frac{1}{s+\gamma+k_u}. \tag{D4}$$

The overall propagator for a particle moving through this system of states can be found by a convolution over all possible transition paths, analogous to the discrete path sampling technique used for calculating kinetics on potential energy surfaces [71]. Specifically, the spatial density of a particle that started at the origin in state i at time 0 and is in state j at time t is given by

$$G_{i,j}(x,t) = \delta_{i,j}F_i + \sum_{n=1}^{\infty}\sum_{k_1,k_2,\ldots,k_n} H_{i,k_1} * \cdots * H_{k_{n-1},k_n} * H_{k_n,j} * F_j, \tag{D5}$$

where n is the number of intermediate states over which the particle transitions and k_l is the identity of the lth intermediate state. Replacing the convolutions with multiplication of the Fourier-Laplace-transformed propagators, we find the overall spatial distribution for a particle that started in a linear combination of initial states described by the vector $\mathbf{P}$,

$$\hat{\tilde{G}}(k,s;\mathbf{P}) = \lim_{\epsilon\to 0}\mathbf{P}\cdot\left(\sum_{n=0}^{\infty}\hat{\tilde{\mathbf{H}}}^n\right)\cdot\hat{\tilde{\mathbf{F}}} = \lim_{\epsilon\to 0}\mathbf{P}\cdot(\mathbf{I}-\hat{\tilde{\mathbf{H}}})^{-1}\cdot\hat{\tilde{\mathbf{F}}}, \tag{D6}$$

where $\mathbf{I}$ is the identity matrix.

The Laplace-transformed mean square displacement can be found directly from the propagator by taking derivatives with respect to k. Its long-time limit is found by expanding to lowest order in s and taking the coefficient of the $1/s^2$ term

$$\lim_{t\to 0}\mathrm{MSD} = \left[-\lim_{s\to 0}s^2\left(\frac{\partial^2}{\partial k^2}\hat{\tilde{G}}(k,s)\Big|_{k=0}\right)\right]t = 2D_{\mathrm{eff}}t, \tag{D7}$$

where the effective long-time diffusivity D_{eff} is given in Eq. (21).

The average time for a particle with initial distribution $\mathbf{P}$ among the different states to first initiate a walk can be found as the time integral of the probability that no walk has yet occurred,

$$\langle t_w(\mathbf{P})\rangle = \int_0^{\infty}dt\int_0^{\infty}dx\; G^*(x,t;\mathbf{P}), \tag{D8}$$

where G^* is obtained from Eq. (D6) with alternate transition matrices $\hat{\tilde{\mathbf{H}}}^*$ and $\hat{\tilde{\mathbf{F}}}^*$ defined by removing the rows and columns of $\hat{\tilde{\mathbf{H}}}$ and $\hat{\tilde{\mathbf{F}}}$ corresponding to the walking state w. The average time to start walking for a particle initially uniformly distributed within the inner radius α can be evaluated as

$$\langle t_w\rangle = [(\mathbf{I}-\hat{\tilde{\mathbf{H}}}^*)^{-1}]_{n_u,\cdot}\cdot\hat{\tilde{\mathbf{F}}}^*\big|_{k=0,s=0}, \tag{D9}$$

where the subscript $n_u,\cdot$ indicates the corresponding row of the inverse matrix. The resulting expression is given in Eq. (22).

We similarly calculate the mean square time to initiate a walk, using

$$\langle t_w^2\rangle = -2\frac{\partial}{\partial s}[(\mathbf{I}-\hat{\tilde{\mathbf{H}}}^*)^{-1}]_{n_u,\cdot}\cdot\hat{\tilde{\mathbf{F}}}^*\big|_{k=0,s=0}. \tag{D10}$$

The variance in the time to start walking is given by $\sigma^2 = \langle t_w^2\rangle - \langle t_w\rangle^2$. While the full closed-form expression is too cumbersome to include here, in the limit of rapid unbinding from the tethered state ($k_u \gg \gamma$ and $k_u \gg D/a^2$), the variance in the walking time is

$$\lim_{k_u\to\infty}\sigma^2 = \frac{4D(1+\alpha^2K_{\mathrm{eq}})^2 - \alpha^2\gamma(3-4\alpha^2+\alpha^4+4\log\alpha)(1+K_{\mathrm{eq}})}{4\alpha^4D\gamma^2(1+K_{\mathrm{eq}})^2}. \tag{D11}$$

Figure 9 shows the Fano factor, a measure of the variability in a stochastic process defined as the standard deviation in the time to start walking, relative to the average time. Large variability in how long it takes a passively diffusing particle to start walking is seen in the case of slow diffusion and strong binding.

APPENDIX E: SIMULATION DETAILS

We simulate moving particles within a cylindrical domain of unit radius and unbounded length. The axial position of each particle is tracked to determine the range and the mean square displacement. We also track the radial position to determine the probability of state transitions for the particles.

Each particle is assigned to a walking, diffusive, or tethered state at initialization. The fraction of particles in each state is determined by the equilibrium distribution given in Eq. (C2). Unbound particles in the diffusive state start uniformly distributed radially throughout the cross section.

We divide the cylindrical domain in two concentric sections [Fig. 6(a)]. The inner domain of radius α denotes the region within which particles can transition from the diffusive state to the walking or tethered state. Particles execute explicit Brownian dynamics with a time step Δt when their radial position is smaller than $3\alpha/2$. This includes the inner domain along with a buffer region of radius $\alpha/2$. The time step is chosen to be smaller than all relevant time scales in the model: $\Delta t \ll \min(1/k_b, 1/\gamma, \alpha^2/2D)$. Note that this choice of time step prevents multiple events occurring within a single step.

Particles outside the capture domain can spend a long time diffusing before reaching the region of interest. To accelerate the simulation, we make use of the first passage time distribution for diffusive particles between two cylindrical boundaries. The cumulative encounter probability to an absorbing inner boundary of radius α with a reflective outer boundary of unit radius is given by

$$\Phi(t) = 1 - \frac{\pi^2}{2}\sum_{n=1}^{\infty}\left[\frac{J_0^2(\beta_n\alpha)\beta_n\alpha}{J_0^2(\beta_n\alpha) - J_1^2(\beta_n)}\right] \times[J_0(\beta_n r)Y_1(\beta_n) - Y_0(\beta_n r)J_1(\beta_n)] \times[Y_1(\beta_n\alpha)J_1(\beta_n) - J_1(\beta_n\alpha)Y_1(\beta_n)]e^{-\beta_n^2 Dt}, \quad \text{(E1)}$$

where J_ν and Y_ν are the Bessel functions of the first and the second kind, respectively, with order ν [70]. The β_n are eigenvalues of the equation $J_1(\beta_n)Y_0(\beta_n\alpha) - J_0(\beta_n\alpha)Y_1(\beta_n) = 0$. The time required to reach the inner domain starting from an initial radial position r is drawn from the above distribution and the particles are propagated along the axis according to the diffusive propagator R_D [Eq. (A1)] over this time interval.

The simulation is run using a hybrid Brownian dynamics–kinetic Monte Carlo algorithm where the probability of a state transition depends on the radial position of the particle. Particles in the diffusive state within the inner domain ($r < \alpha$) can transition to the tethered or walking states at a combined rate $k_b + \gamma$. A transition is attempted at every diffusion time step based on the relative probabilities for tethering and walking. Transitions leading away from the tethered state occur with a rate k_u to the diffusive state and with a rate γ to the walking state. Particles in the walking state transition to the diffusive state a rate λ. Each time particles reenter the diffusive state they are uniformly distributed in the radial dimension within the inner region (of radius α), ensuring symmetry between the binding and unbinding positions. A schematic of these transitions is shown in Fig. 6(a). For each transition out of a tethered or walking state, the waiting time is drawn from an exponential distribution with the mean equal to the corresponding transition rate. The particles are propagated in space according to the distribution for the given state over the duration of the waiting time. The simulation continues until all particles have covered a predetermined time interval.

[1] M.-M. Fu and E. L. Holzbaur, Trends Cell Biol. **24**, 564 (2014).
[2] J. Salogiannis, M. J. Egan, and S. L. Reck-Peterson, J. Cell Biol. **212**, 289 (2016).
[3] C. Kural, A. S. Serpinskaya, Y.-H. Chou, R. D. Goldman, V. I. Gelfand, and P. R. Selvin, Proc. Natl. Acad. Sci. USA **104**, 5378 (2007).
[4] J. L. Ross, M. Y. Ali, and D. M. Warshaw, Curr. Opin. Cell. Biol. **20**, 41 (2008).
[5] H. V. Mudrakola, K. Zhang, and B. Cui, Structure **17**, 1433 (2009).
[6] Š. Bálint, I. V. Vilanova, Á. S. Álvarez, and M. Lakadamyali, Proc. Natl. Acad. Sci. USA **110**, 3375 (2013).
[7] W. O. Hancock, Nat. Rev. Mol. Cell Biol. **15**, 615 (2014).
[8] C. P. Brangwynne, G. H. Koenderink, F. C. MacKintosh, and D. A. Weitz, Trends Cell Biol. **19**, 423 (2009).
[9] M. Mussel, K. Zeevy, H. Diamant, and U. Nevo, Biophys. J. **106**, 2710 (2014).
[10] K. Jaqaman, H. Kuwata, N. Touret, R. Collins, W. S. Trimble, G. Danuser, and S. Grinstein, Cell **146**, 593 (2011).
[11] V. Ananthanarayanan, M. Schattat, S. K. Vogel, A. Krull, N. Pavin, and I. M. Tolić-Nørrelykke, Cell **153**, 1526 (2013).
[12] A. Godec and R. Metzler, Phys. Rev. E **92**, 010701 (2015).
[13] S. Klumpp and R. Lipowsky, Phys. Rev. Lett. **95**, 268102 (2005).
[14] M. J. Müller, S. Klumpp, and R. Lipowsky, Biophys. J. **98**, 2610 (2010).
[15] L. Bruno, V. Levi, M. Brunstein, and M. A. Desposito, Phys. Rev. E **80**, 011912 (2009).
[16] D. Campos, E. Abad, V. Mendez, S. B. Yuste, and K. Lindenberg, Phys. Rev. E **91**, 052115 (2015).
[17] A. Kahana, G. Kenan, M. Feingold, M. Elbaum, and R. Granek, Phys. Rev. E **78**, 051912 (2008).
[18] C. Loverdo, O. Bénichou, M. Moreau, and R. Voituriez, Nat. Phys. **4**, 134 (2008).
[19] O. Bénichou, C. Loverdo, M. Moreau, and R. Voituriez, Rev. Mod. Phys. **83**, 81 (2011).
[20] Y. Tanaka, Y. Kanai, Y. Okada, S. Nonaka, S. Takeda, A. Harada, and N. Hirokawa, Cell **93**, 1147 (1998).
[21] C. Kural, H. Kim, S. Syed, G. Goshima, V. I. Gelfand, and P. R. Selvin, Science **308**, 1469 (2005).
[22] M. Schuster, R. Lipowsky, M.-A. Assmann, P. Lenz, and G. Steinberg, Proc. Natl. Acad. Sci. USA **108**, 3618 (2011).
[23] P. Targett-Adams *et al.*, J. Biol. Chem. **278**, 15998 (2003).
[24] C. Lin, M. Schuster, S. C. Guimaraes, P. Ashwin, M. Schrader, J. Metz, C. Hacker, S. J. Gurr, and G. Steinberg, Nat. Commun. **7**, 11814 (2016).
[25] D. T. Chang, A. S. Honick, and I. J. Reynolds, J. Neurosci. **26**, 7035 (2006).
[26] A. M. Valm, S. Cohen, W. R. Legant, J. Melunis, U. Hershberg, E. Wait, A. R. Cohen, M. W. Davidson, E. Betzig, and J. Lippincott-Schwartz, Nature (London) **546**, 162 (2017).

[27] N. Hirokawa and R. Takemura, Nat. Rev. Neurosci. **6**, 201 (2005).
[28] M. A. De Matteis and A. Luini, Nat. Rev. Mol. Cell Biol. **9**, 273 (2008).
[29] I. Singh, Mol. Cell. Biochem. **167**, 1 (1997).
[30] N. A. Bright, M. J. Gratian, and J. P. Luzio, Curr. Biol. **15**, 360 (2005).
[31] P. C. Bressloff and J. M. Newby, Rev. Mod. Phys. **85**, 135 (2013).
[32] J. Gou, L. Edelstein-Keshet, and J. Allard, Mol. Biol. Cell. **25**, 2408 (2014).
[33] D. Ando, N. Korabel, K. C. Huang, and A. Gopinathan, Biophys. J. **109**, 1574 (2015).
[34] L. S. Goldstein and Z. Yang, Annu. Rev. Neurosci. **23**, 39 (2000).
[35] M. J. Egan, M. A. McClintock, and S. L. Reck-Peterson, Curr. Opin. Microbiol. **15**, 637 (2012).
[36] X.-A. Liu, V. Rizzo, and S. Puthanveettil, J. Transl. Neurosci. **3**, 355 (2012).
[37] J. R. Cooper and L. Wordeman, Curr. Opin. Cell Biol. **21**, 68 (2009).
[38] T. L. Culver-Hanlon, S. A. Lex, A. D. Stephens, N. J. Quintyne, and S. J. King, Nat. Cell Biol. **8**, 264 (2006).
[39] J.-S. Kang, J.-H. Tian, P.-Y. Pan, P. Zald, C. Li, C. Deng, and Z.-H. Sheng, Cell **132**, 137 (2008).
[40] G. Pekkurnaz, J. C. Trinidad, X. Wang, D. Kong, and T. L. Schwarz, Cell **158**, 54 (2014).
[41] R. L. Frederick and J. M. Shaw, Traffic **8**, 1668 (2007).
[42] M. J. Müller, S. Klumpp, and R. Lipowsky, Proc. Natl. Acad. Sci. USA **105**, 4609 (2008).
[43] L. G. Leal, *Advanced Transport Phenomena: Fluid Mechanics and Convective Transport Processes* (Cambridge University Press, Cambridge, 2007).
[44] D. Bandyopadhyay, A. Cyphersmith, J. A. Zapata, Y. J. Kim, and C. K. Payne, PLoS One **9**, e86847 (2014).
[45] A. G. Hendricks, E. Perlson, J. L. Ross, H. W. Schroeder III, M. Tokito, and E. L. Holzbaur, Curr. Biol. **20**, 697 (2010).
[46] A. D. Pilling, D. Horiuchi, C. M. Lively, and W. M. Saxton, Mol. Biol. Cell. **17**, 2057 (2006).
[47] W. W. Ahmed and T. A. Saif, Sci. Rep. **4**, 4481 (2014).
[48] E. V. Romanova, S. P. Oxley, S. S. Rubakhin, P. W. Bohn, and J. V. Sweedler, Biomaterials **27**, 1665 (2006).
[49] S. E. Encalada, L. Szpankowski, C.-H. Xia, and L. S. Goldstein, Cell **144**, 551 (2011).
[50] K. Chen, B. Wang, J. Guan, and S. Granick, ACS Nano **7**, 8634 (2013).
[51] W. Feller, Ann. Math. Statist. **12**, 243 (1941).
[52] A. Talbot, IMA J. Appl. Math. **23**, 97 (1979).
[53] P. Danckwerts, Appl. Sci. Res. A **3**, 279 (1952).
[54] Z. Stone and H. Stone, Phys. Fluids **17**, 063103 (2005).
[55] J.-L. Thiffeault, Nonlinearity **25**, R1 (2012).
[56] P. Ashwin, M. Nicol, and N. Kirkby, Physica A **310**, 347 (2002).
[57] M. Camesasca, M. Kaufman, and I. Manas-Zloczower, Macromol. Theor. Simul. **15**, 595 (2006).
[58] S. Redner, *A Guide to First-Passage Processes* (Cambridge University Press, Cambridge, 2001).
[59] K. Ogawa and S. Ito, J. Chem. Eng. Jpn. **8**, 148 (1975).
[60] G. Jedd and N.-H. Chua, Nat. Cell Biol. **2**, 226 (2000).
[61] J. L. Ross, H. Shuman, E. L. Holzbaur, and Y. E. Goldman, Biophys. J. **94**, 3115 (2008).
[62] S. R. Chada and P. J. Hollenbeck, Curr. Biol. **14**, 1272 (2004).
[63] S. J. Peter and M. R. Mofrad, Biophys. J. **102**, 749 (2012).
[64] A. Straube, G. Hause, G. Fink, and G. Steinberg, Mol. Biol. Cell. **17**, 907 (2006).
[65] M. Schuster, S. Kilaru, G. Fink, J. Collemare, Y. Roger, and G. Steinberg, Mol. Biol. Cell. **22**, 3645 (2011).
[66] R. García-Pelayo, J. Phys. A **38**, 3475 (2005).
[67] D. St Johnston, Nat. Rev. Mol. Cell Biol. **6**, 363 (2005).
[68] C. Loverdo, O. Bénichou, M. Moreau, and R. Voituriez, J. Stat. Mech. (2009) P02045.
[69] E. F. Koslover, M. A. D. de la Rosa, and A. J. Spakowitz, Biophys. J. **101**, 856 (2011).
[70] M. N. Ozisik, *Heat Transfer: A Basic Approach* (McGraw-Hill, New York, 1985).
[71] D. J. Wales, Mol. Phys. **100**, 3285 (2002).